# LATVIAN JOURNAL of PHYSICS and TECHNICAL SCIENCES

ISSN 0868 - 8257

6

(Vol. 59)

2022

CONTENTS

# LATVIAN JOURNAL of PHYSICS and TECHNICAL SCIENCES

# LATVIJAS FIZIKAS un TEHNISKO ZINĀTŅU ŽURNĀLS

# ЛАТВИЙСКИЙ ФИЗИКО-ТЕХНИЧЕСКИЙ ЖУРНАЛ

Published six times a year since February 1964
Iznāk sešas reizes gadā kopš 1964. gada februāra
Выходит шесть раз в год с февраля 1964 года

6 (Vol. 59) • 2022

RĪGA

Language Editor: O. Ivanova
Computer Designer: I. Begicevs

INDEXED (PUBLISHED) IN

www.scopus.com
www.sciendo.com
EBSCO (Academic Search Complete, www.epnet.com), INSPEC (www.iee.org.com).
VINITI (www.viniti.ru), Begell House Inc/ (EDC, www.edata-center.com).

Issuers: Institute of Physical Energetics,
Institute of Solid State Physics, University of Latvia
Registration Certificate Number: 000700221

Editorial Contacts:
14 Dzerbenes Street, Riga, LV - 1006
Ph.: + 371 67551732
E-mail: leo@lza.lv
www.fei-web.lv

sciendo

LATVIAN JOURNAL OF PHYSICS
AND TECHNICAL SCIENCES
2022, N 6

DOI: 10.2478/lpts-2022-0042

# DFT SIMULATIONS OF $Zn_xMg_{1-x}O$ SOLID SOLUTIONS FOR SOLAR-BLIND UV SENSORS: EVALUATION OF ELECTRONIC STRUCTURE AND PHASE STABILITY

S. Piskunov[1,*], O. Lisovski[1], A. Gopejenko[1], L. Trinkler[1],
M.M.C. Chou[2], L.W. Chang[2]

[1] Institute of Solid State Physics, University of Latvia,
8 Kengaraga Str., Riga, LV-1063, LATVIA
[2] Center of Crystal Research,
Department of Materials and Optoelectronic Science,
National Sun Yat-Sen University,
70 Lianhai Rd, Gushan District, Kaohsiung City, TAIWAN
*e-mail: piskunov@cfi.lu.lv

In this research, density functional theory accompanied with linear combination of atomic orbitals (LCAO) method is applied to study the atomic and electronic structure of wurtzite and rocksalt $Zn_xMg_{1-x}O$ pseudobinary compounds in their bulk phases. Calculated band gaps of $Zn_xMg_{1-x}O$ solid solutions under study are further validated by means of spectroscopic ellipsometry and optical absorption. In agreement with an experiment, it is predicted that increase of Zn content in $Zn_xMg_{1-x}O$ leads to narrowing of its band gap for both wurtzite and rocksalt phases. The calculated infra-red (IR) spectra show that the IR peaks are shifted towards larger frequencies along with decrease of Zn content. Presence of imaginary phonon frequencies in rocksalt $Zn_xMg_{1-x}O$ of $x > 0.625$ allows us to suggest that it is necessary to use properly oriented substrates for epitaxial growth to overcome polycrystallinity in$Zn_xMg_{1-x}O$ thin films at concentration $x = 0.4 – 0.6$.

***Keywords:*** *Calculated IR spectra, density functional theory, electronic structure, solid solutions,* $Zn_xMg_{1-x}O$.

## 1. INTRODUCTION

Deep UV photon sensors based on wide or ultrawide-bandgap semiconductors, such as II-oxides, III-nitrides, diamond, and SiC can be used extensively in numerous applications such as biological and chemical sensors for ozone detection, water purification, determination of pollution levels in air or any biological agent, and in aerospace missions. However, more and more applications require a photosensing device/system enabling discrimination between emitting or polluting species. Bandgaps ($E_g$) of some semiconductors, such as diamond and SiC, are not tunable, and those of other semiconductors, such as composite III-nitrides can only be varied from 3.4 eV to less than 4.5 eV. Other UV photon sensors have been fabricated using various ultra-wide bandgap semiconductors such as β-$Ga_2O_3$ ($E_g$ = 4.9 eV) [1], AlN ($E_g$ = 6.0 eV) [2], diamond ($E_g$ = 5.5 eV) [3, 4], and BN (Eg = 6.4 eV) [5]. These photodetectors usually suffer from slow response time, low spectral selectivity and high dark current.

Incorporation of more than 50 % of a foreign metal is one of the discussed problems [6]. The situation is similar for wurtzite $Zn_xMg_{1-x}O$ (ZMO). It is known that the ZMO films having the x value higher than 0.4 usually consist of a mixture of rocksalt (rs) and wurtzite (wz) phases due to phase separation, which also limits the bandgap value to about 4.3 eV [7]–[10]. A new deep UV detector based on a ZnO-MgO pseudobinary semiconductor with either a pure wz or rs crystal structure, in turn, would have a tunable bandgap from 3.3 to 7.8 eV and an operating energy range from 4.0 eV to 6.0 eV, thus significantly enhancing the capabilities of the devices at different energies simultaneously. Wen et al. [11] indicated that the limitation of ZnO and MgO mutual solubilities could be broken by stabilizing the high MgO-content wz-ZMO and high ZnO-content rs-ZMO by using low lattice mismatch substrates such as $ScAlMgO_4$, MgO and $Cu_2O$. Such devices will have advantages of small size, low operating voltage, and low cost. However, the success of these devices relies on a thorough understanding of the basic microstructural, optical and electric properties of the materials and the heterojunctions. It should be noted here that while the UV and VUV photon induced processes have been studied in detail both in MgO [12]–[14] and in ZnO [15]–[17], the corresponding phenomena in their mixed compositions are still far from being understood [18].

Recently it has been demonstrated that rs-ZMO epilayers and heterostructures can be grown on MgO (100) substrates with the x value as low as 0.17–0.30 [19]–[23]. The rs-ZMO epilayers thus exhibit band gap of 4.5 eV and above. It is also known that the addition of MgO in wurtzite ZnO (wz-ZnO) can be over the limit of 40 % suggested previously and reach a high value of 70 % as a lattice-matched substrate if $ScAlMgO_4$ (SCAM) is used [24]. Apart from experimental studies consisting in establishing growth techniques, large-scale computer modelling of crystalline ZMO heterostructures is needed in order to predict their electronic band structure, stability and vibrational properties of the wz and rs phases with respect to ZMO atomic composition. In particular, it is important to investigate phase stability of both wz- and rs-ZMO compounds in order to evaluate potential of low lattice mismatch substrate applicability. Theoretical computer modelling of ZMO alloys have been carried out within the past

decade to investigate morphology of their bulk phase transitions and the fundamental electronic structure [25], [26]. It should also be noted that simulations of these materials are considerably less numerous than those of more common materials, such as $TiO_2$. As one more of the few examples, Xu He et al. [27] used the GGA+U method to study ZMO to be used as a window layer material in CdTe solar cells. They observed that increasing of Mg content led to broadening of the band gap [27]. The same authors also studied a similar system with In doping [27]. Unfortunately, a specific goal of their research did not allow drawing direct parallels. Another group [28] also performed calculations of ZMO, but the set of x value was limited to 0.25 and 0.5.

However, in ZMO epilayers not only the bulk properties, but also interfaces play an essential role. Therefore, a correct description of ZMO solid solutions, their vibrational properties, and their electronic structure, positions of the band edges are necessary for predicting ZMO material properties, besides confirming and explaining experimental results. In this study, we use density functional theory (DFT) for simulation of both wz- and rs-ZMO with x in the range from 0.125 to 0.875 in order to investigate phase stability, vibrational properties and bang gap behavior with respect to Zn/Mg content. The calculated values of band gap width are compared with those experimentally measured.

## 2. COMPUTATIONAL DETAILS

Simulations of ZMO solid solution with x varying by 0.125 increment are performed on both wz and rs phases using hybrid DFT LCAO method. This approach utilizes localized Gaussian-type functions (GTFs) in the form of basis set (BS) centered on atomic nuclei for expansion of crystalline orbitals as linear combinations of atomic orbitals (CO-LCAO), as it is implemented in the total energy code CRYSTAL [29]. CRYSTAL possesses a feature of symmetry exploitation, which considerably reduces the computational costs. In this study, we have calculated electronic band structures, atomic structures, and IR spectra of both wz- and rs-ZMO solid solutions under study. The hybrid exchange-correlation functional PBE0 has been used [29]. The Triple-Zeta Valence with polarization quality BSs for Mg has been taken from [30], while for Zn and O BSs it has been taken according to prescriptions given in [31].

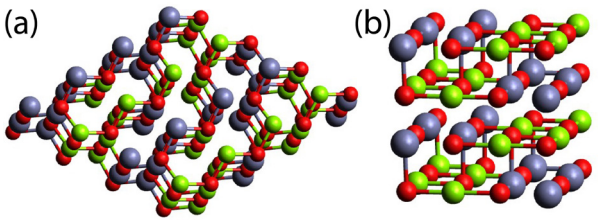


*Fig. 1.* Schematic representation of equilibrium ZMO supercells in (a) wurtzite and (b) rocksalt phases with concentration of x=0.5. Grey balls denote Zn, green – Mg, red – O. Each supercell contains 64 atoms.

In order to simulate the ZMO solid solutions, the corresponding wz or rs unit cell was expanded to a 2×2×2 SC. The SC retains the symmetry of host wz or rs phases and contains 64 atoms (Fig. 1). For all studied ZMO structures, the equilibrium geometry

is obtained using an analytical optimization method as implemented in the CRYSTAL code [29]. To provide a balanced summation in both direct and reciprocal lattices, the reciprocal space integration has been performed by sampling the SC's Brillouin zone with a 6×6×6 Pack-Monkhorst mesh [32]. Calculations have been considered as converged only when the total energy differs by less than 108 a.u. in two successive cycles of the self-consistent field (SCF) procedure. The total geometry optimization has been performed by keeping the corresponding bulk symmetry fixed. Within the self-consistency, the accuracies (tolerances) of $10^{-8}$ have been chosen for calculations of Coulomb and exchange integrals [29]. Band gaps calculated for ZMO parent materials, wz-ZnO ($E_g$ = 3.57 eV) and rs-MgO ($E_g$ = 7.34 eV), are in good agreement with those experimentally measured – 3.37 eV [33] and 7.77 eV [34], respectively.

## 3. EXPERIMENT

In this study, we have done characterization of the band gaps of ZMO materials (thin films). Optical properties (band gaps) have been obtained by means of spectroscopic ellipsometer (SE) WOOLLAM RC2 in the spectral range from 210 to 1690 nm (or from 5.9 to 0.7 eV). In addition, temperature-dependant absorption (TDA) has been measured for ZMO samples under study by means of spectrophotometer Analytic Jena Specord 210; low temperatures have been provided by refrigerator Janis (10–300 K). Both wz- and rs-ZMO thin film samples have been produced in Taiwan, Sun Yat Sen University [11], [24]. Rock salt ZMO thin films were synthesized on MgO substrate by means of molecular beam epitaxy (MBE) with the x value of 0.35, 0.5, 0.63, 0.72, 0.82, and 0.87. Wurtzite ZMO thin films have been grown by means of MBE on SCAM substrate and have concentration x = 0.34, 0.5, 0.56, and 0.74.

## 4. RESULTS AND DISCUSSION

A series of PBE calculations has been done for both wz and rs ZMO phases, varying concentration x from 0.125 to 0.875 with 0.125 increment. Top of the valence band (VB) of wz- and rs-ZMO consists mainly of O 2p orbitals with a small admixture of Zn 3d states. As the concentration x is increased, the Zn 3d–O 2p hybridisation becomes more pronounced. The bottom of the conduction band (CB) is essentially comprised of the 2p orbitals associated with the oxygen atoms and zinc 3d orbitals. In agreement with [35], our calculations predict direct band gap for wz-ZMO solid solutions under study, while indirect optical gap has been calculated for rs-ZMO.

The calculated band gap for pristine wz-ZnO bulk is 3.57 eV (compared to 3.37 eV experiment [33]). It gradually grows up to 5.86 eV at x = 0.125 of wz-ZMO (Table 1). The growth is mostly attributed to CB bottom shift to higher energies, although the VB top is also slightly shifted towards more negative energies. The calculated band gap for pristine rs-MgO bulk is 7.34 eV (compared to experimental value of 7.8 eV [34]). It gradually gets narrower and reaches 3.84 eV at 87.5 % Zn concentration. The shift is more prominent in the CB bottom than in the VB top. Band gap narrowing

with increased Zn concentration in ZMO solid solution is attributed to Zn 3d – O 2p orbital hybridization. Calculated $E_g$ values for wz- and rs-ZMO listed in Table 1 are in line with those measured by means of spectroscopic ellipsometry and temperature-dependent absorption.

**Table 1.** Calculated by Means of PBE0 DFT and Measured by eans of Temperature-Dependent Absorption (TDA) and Spectroscopic Ellipsometry (SE) band Gaps (Eg) of Both wz and rs ZMO vs. Varying Concentration x of ZnO

| | wz ZMO | | | rs ZMO | | |
|---|---|---|---|---|---|---|
| x | DFT | SE | TDA | DFT | SE | TDA |
| 0.125 | 5.86 | | | 5.80 | | |
| 0.25 | 5.55 | | | 5.37 | | |
| 0.35 | | 4.30 | 4.30 | | 5.58 | 5.5 |
| 0.375 | 5.20 | | | 4.89 | | |
| 0.5 | 4.81 | 4.00 | 4.20 | 4.76 | 4.82 | 5.2 |
| 0.56 | | 3.72 | 4.0 | | | |
| 0.625 | 4.41 | | | 4.30 | 5.03 | 5.10 |
| 0.72 | | | | | 4.51 | 5.00 |
| 0.75 | 4.15 | 3.75 | 3.80 | 4.17 | | |
| 0.82 | | | | | | 4.60 |
| 0.875 | 3.86 | | | 3.84 | | 4.30 |

IR spectra were calculated for each incremental point on the 0–100% scale of both wz- and rs-ZMO (Fig. 2). In Fig. 2, we limit ourselves to showing results for 4 various structures to illustrate the trend. The calculated IR spectra for the bulk wz ZnO and x = 0.875 wz ZMO exhibit a slight shift of the peak 425 $cm^{-1}$ towards larger wavenumbers for the latter (Fig. 2a). Further decrease of Zn content shifts the peaks further to the right. With x = 0.5 ZMO exhibits no single dominating peak but rather several peaks of approximately equal intensity. When concentration reaches x = 0.125, in spectrum a new dominating double peak appears at larger wavenumbers of 550 $cm^{-1}$ (Fig. 2a). In the case of the rs-ZMO, for the pristine bulk the graph has a single dominating peak at larger wavenumbers (450 $cm^{-1}$). Gradually adding Zn atoms, one can observe that intensity of the peak gets lower reaching a minimum for 87.5 % Zn concentration. A shift towards smaller wavenumbers is also predicted. For x = 0.125, the dominating peak becomes double and this effect develops until there is no prominent dominating peak or group of peaks for the x = 0.875 (Fig. 2b).

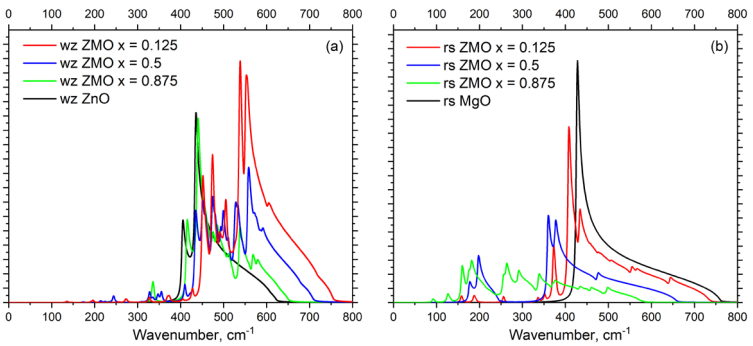


*Fig. 2.* Calculated IR spectra of (a) wz and (b) rs ZMO of x = 0, 0.125, 0.5, 0.875, and 1.

An important part of this study is evaluation of stability of the wz and rs structures of ZMO. One of the approaches is to investigate presence of imaginary phonon frequencies. In the case of the wz structure, no imaginary frequencies were calculated regardless of Mg concentration. This means that the wz phase of ZMO have high potential of being stabilized on low-lattice mismatch substrate with x varying in 0–1 interval. In turn, for the rs structure, it is predicted that imaginary frequencies can appear when concentration of Zn reaches 62.5 %, which gives a ground for predicting further stability of rs-ZMO phase if an appropriate substrate for the x in 0–0.5 interval will be proposed.

## 5. CONCLUSIONS

In this study, we have performed first-principle calculation of both rs and wz phases of ZMO solid solutions with concentration x varying from 0.125 to 0.875 with an increment of 0.125. It has been found that due to Zn 3d–O 2p orbital hybridization, an increase of Zn content in ZMO leads to narrowing of band gaps for both wz and rs phases, which is in agreement with measured data. In the calculated density of state (DOS), no appearance of additional peaks inside the band gap is predicted, while the VB and CB edge positions are shifted. The calculated IR spectra show that the peaks are shifted towards larger frequencies with a decrease of Zn content in both wz and rs ZMO pseudobinary compounds. Finally, imaginary frequencies are totally absent in case of wz-ZMO and are also absent for rs-ZMO with Zn content up to 62.5 %. The structures with the absence of the imaginary phonon frequency are thermodynamically stable and are able to overcome mutual solubility problem, thus being promising candidates for experimental growth on substrates with now lattice mismatch. Further stabilization of the rs-ZMO with $x > 0.625$ can be made by the use of local lattice stress by selection of proper substrate (or their crystallographic orientation) during the growth of ZMO thin films.

## ACKNOWLEDGMENTS

The financial support of M-ERA.NET project “ZnMgO Materials with Tunable Band Gap for Solar-Blind UV Sensors” (ZMOMUVS) is greatly acknowledged. The Institute of Solid State Physics, University of Latvia, as the Centre of Excellence, has received funding from the European Union’s Horizon 2020 Framework Program H2020-WIDESPREAD-01-2016-2017-TeamingPhase2 under Grant Agreement No. 739508, project CAMART$^2$.

## REFERENCES

1. Wu, Z., Bai, G., Qu, Y., Guo, D., Li, L., Li, P., … & Tang, W. (2016). Deep Ultraviolet Photoconductive and Near-Infrared Luminescence Properties of $Er^{3+}$-Doped β-$Ga_2O_3$ Thin Films. *Applied Physics Letters*, *108*, 211903. DOI: 10.1063/1.4952618

2. Wu, P., Funato, M., & Kawakami, Y. (2015). Environmentally Friendly Method to Grow Wide-Bandgap Semiconductor Aluminum Nitride Crystals: Elementary Source Vapor Phase Epitaxy. *Scientific reports*, *5*, 1–9. DOI: 10.1038/srep17405
3. Koide, Y., Liao, M., Alvarez, J., Imura, M., Sueishi, K., & Yoshifusa, F. (2009). Schottky Photodiode Using Submicron Thick Diamond Epilayer for Flame Sensing. *Nano-Micro Letters*, *1*, 30–33. DOI: 10.1007/BF03353603
4. Liao, M., Sang, L., Teraji, T., Imura, M., Alvarez, J., & Koide, Y. (2012). Comprehensive Investigation of Single Crystal Diamond Deep-Ultraviolet Detectors. *Japanese Journal of Applied Physics*, *51*, 090115. DOI: 10.1143/JJAP.51.090115
5. Aldalbahi, A., & Feng, P. (2015). Development of 2-D Boron Nitride Nanosheets UV Photoconductive Detectors. *IEEE Transactions on Electron Devices*, *62*, 1885–1890. DOI: 10.1109/TED.2015.2423253
6. Vennegues, P., Bougrioua, Z., Bethoux, J., Azize, M., & Tottereau, O. (2005). Relaxation Mechanisms in Metal-Organic Vapor Phase Epitaxy Grown Alrich (Al,Ga)N\GaN Heterostructures. *Journal of Applied Physics*, *97*, 024912.DOI: 10.1063/1.1828607
7. Koike, K., Hama, K., Nakashima, I., Takada, G.-y., Ogata, K.-i., Sasa, S., … & Yano, M. (2005). Molecular Beam Epitaxial Growth of Wide Bandgap ZnMgO Alloy Films on (111)-Oriented Si Substrate toward UV-Detector Applications. *Journal of Crystal Growth*, *278*, 288–292. DOI: 10.1016/j.jcrysgro.2005.01.021
8. Fan, M., Liu, K., Zhang, Z., Li, B., Chen, X., Zhao, D., … & Shen, D. (2014). High-Performance Solar-Blind Ultraviolet Photodetector Based on Mixed-Phase ZnMgO Thin Film. *Applied Physics Letters*, *105*, 011117. DOI: 10.1063/1.4889914
9. Mayes, E., Murdoch, B., Bilek, M., McKenzie, D., McCulloch, D., & Partridge, J. (2015). Co-deposition of Band-Gap Tuned $Zn_{1-x}Mg_xO$ Using High Impulse Power- and DC-Magnetron Sputtering. *Journal of Physics D: Applied Physics*, *48*, 135301. DOI: 10.1088/0022-3727/48/13/135301
10. Takeuchi, I., Yang, W., Chang, K.-S., Aronova, M., Venkatesan, T., Vispute, R., & Bendersky, L. (2003). Monolithic Multichannel Ultraviolet Detector Arrays and Continuous Phase Evolution in $Mg_xZn_{1-x}O$ Composition Spreads. *Journal of Applied Physics*, *94*, 7336–7340. DOI: 10.1063/1.1623923
11. Wen, M., Lu, S., Chang, L., Chou, M., & Ploog, K., (2017). Epitaxial Growth of Rocksalt $Zn_{1-x}Mg_xO$ on MgO (100) Substrate by Molecular Beam Epitaxy. *Journal of Crystal Growth*, *477*, 169–173. DOI: 10.1016/j.jcrysgro.2017.01.023
12. Gonzalez, R., Monge, M., Santiuste, J.M., Pareja, R., Chen, Y., Kotomin, E., ... & Popov, A. (1999). Photoconversion of F-type Centers in Thermochemically Reduced MgO Single Crystals. *Physical Review B*, *59*, 4786. DOI: 10.1103/PhysRevB.59.4786
13. Monge, M., Gonzalez, R., Santiuste, Pareja, R., Chen, Y., Kotomin, E., & Popov, A. (1999). Photoconversion and Dynamic Hole Recycling Process in Anion Vacancies in Neutron-Irradiated MgO Crystals. *Physical Review B*, *60*, 3787. DOI: 10.1103/PhysRevB.60.3787
14. Monge, M., Gonzalez, R., Santiuste, J.M., Pareja, R., Chen, Y., Kotomin, E., & Popov, A. (2000). Photoconversion of $F^+$ Centers in Neutron-Irradiated MgO. *Nuclear Instruments and Methods in Physics Research Section B: Beam Interactions with Materials and Atoms*, *166*, 220–224. DOI: 10.1016/S0168-583X(99)00751-X
15. Khaliullin, S.M., Zhuravlev, V., Ermakova, L., Buldakova, L.Y., Yanchenko, M.Y., & Porotnikova, N. (2019). Solution Combustion Synthesis of ZnO Using Binary Fuel (Glycine + Citric Acid). *International Journal of Self-Propagating High-Temperature Synthesis*, *28*, 226–232. DOI: 10.3103/S1061386219040058
16. Grigorjeva, L., Millers, D., Smits, K., Pankratov, V., Lojkowski, W., Fidelus, J., … & Monty, C. (2009). Excitonic Luminescence in ZnO Nanopowders and Ceramics. *Optical Materials*, *31*, 1825–1827. DOI: 10.1016/j.optmat.2008.10.052

17. Uklein, A., Multian, V., Kuz'micheva, G., Linnik, R., Lisnyak, V., Popov, A., & Gayvoronsky, V.Y. (2018). Nonlinear Optical Response of Bulk ZnO Crystals with Different Content of Intrinsic Defects. *Optical Materials*, *84*, 738–747. DOI: 10.1016/j.optmat.2018.08.001

18. Babu, K. S., Reddy, A. R., & Reddy, K. V. (2015). Green Emission from ZnO–MgO Nanocomposite due to Mg Diffusion at the Interface. *Journal of Luminescence, 158*, 306–312.

19. Wang, L., Ma, J., Xu, H., Zhang, C., Li, X., & Liu, Y. (2013). Anisotropic Strained Cubic MgZnO/MgO Multiple-Quantum-Well Nanorods: Growths and Optical Properties. *Applied Physics Letters*, *102*, 031905. DOI: 10.1063/1.4788685

20. Lu, C.-Y.J., Tu, Y.-T., Yan, T., Trampert, A., Chang, L., & Ploog, K. (2016). Growth and Stability of Rocksalt $Zn_{1-x}Mg_xO$ Epilayers and ZnO/MgO Superlattice on MgO (100) Substrate by Molecular Beam Epitaxy. *The Journal of Chemical Physics*, *144*, 214704. DOI: 10.1063/1.4950885

21. Wang, L., Ju, Z., Shan, C., Zheng, J., Li, B., Zhang, Z., … & Zhang, J. (2010). Epitaxial Growth of High Quality Cubic MgZnO Films on MgO Substrate. *Journal of Crystal Growth*, *312*, 875–877. DOI: 10.1016/j.jcrysgro.2010.01.009

22. Liang, H., Mei, Z., Liu, Z., Guo, Y., Azarov, A.Y., Kuznetsov, A.Y., ... & Du, X. (2012). Growth of Single-Phase $Mg_{0.3}Zn_{0.7}O$ Films Suitable for Solar-Blind Optical Devices on RS-MgO Substrates. *Thin Solid Films*, *520*, 1705–1708. DOI: 10.1016/j.tsf.2011.08.019

23. Lu, C.-Y., Yan, T., Chang, L., Ploog, K., Chou, M., & Chiang, C.-M. (2013). Rocksalt $Zn_{1-x}Mg_xO$ Epilayer Having High Zn Content Grown on MgO (100) Substrate by Plasma-Assisted Molecular Beam Epitaxy. *Journal of Crystal Growth*, *378*, 168–171. DOI: 10.1016/j.jcrysgro.2012.12.053

24. Wen, M., Yan, T., Chang, L., Chou, M., Ye, N., & Ploog, K. (2017). Achieving High MgO Content in Wurtzite ZnO Epilayer Grown on $ScAlMgO_4$ Substrate. *Journal of Crystal Growth*, *477*, 174–178. DOI: 10.1016/j.jcrysgro.2016.12.031

25. Maznichenko, I., Ernst, A., Bouhassoune, M., Henk, J., Dane, M., Lueders, M., … & Temmerman, W.M. (2009). Structural Phase Transitions and Fundamental Band Gaps of $Mg_xZn_{1-x}O$ Alloys from First Principles. *Physical Review B*, *80*, 144101. DOI: 10.1103/PhysRevB.80.144101

26. Djelal, A., Chaibi, K., Tari, N., Zitouni, K., & Kadri, A. (2017). Ab-initio DFT-FPLAPW/TB-mBJ/LDA-GGA Investigation of Structural and Electronic Properties of $Mg_xZn_{1-x}O$ Alloys in Wurtzite, Rocksalt and Zinc-Blende Phases. *Superlattices and Microstructures*, *109*, 81–98. DOI: 10.1016/j.spmi.2017.04.041

27. Xu, H., Sheng-Qiang, R., Chun-Xiu, L., Li-Li, W., Jing-Quan, Z., & Zheng, D. (2018). $Zn_{1-x}Mg_xO$: Band Structure and Simulation as Window Layer for CdTe Solar Cell by SCAPS Software. *Journal of Inorganic Materials*, *33*, 635–640. DOI: 10.15541/jim20170349

28. Bhadram, V.S., Cheng, Q., Chan, C.K., Liu, Y., Lany, S., Landskron, K., & Strobel, T.A. (2018). $Zn_xMn_{1-x}O$ Solid Solutions in the Rocksalt Structure: Optical, Charge Transport, and Photoelectrochemical Properties. *ACS Applied Energy Materials*, *1*, 260–266. DOI: 10.1021/acsaem.7b00084

29. Dovesi, R., Erba, A., Orlando, R., Zicovich-Wilson, C.M., Civalleri, B., Maschio, L., … & Kirtman, B. (2018). Quantum-Mechanical Condensed Matter Simulations with CRYSTAL. *Wiley Interdisciplinary Reviews: Computational Molecular Science*, *8*, e1360. DOI: 10.1002/wcms.1360

30. Peintinger, M.F., Oliveira, D.V., & Bredow, T. (2013). Consistent Gaussian Basis Sets of Triple-Zeta Valence with Polarization Quality for Solid-State Calculations. *Journal of Computational Chemistry*, *34*, 451–459. DOI: 10.1002/jcc.23153

31. Gryaznov, D., Blokhin, E., Sorokine, A., Kotomin, E.A., Evarestov, R.A., Bussmann-Holder, A., & Maier, J. (2013). A Comparative Ab Initio Thermodynamic Study of Oxygen Vacancies in ZnO and $SrTiO_3$: Emphasis on Phonon Contribution. *The Journal of Physical Chemistry C*, *117*, 13776–13784. DOI: 10.1021/jp400609e

32. Monkhorst, H.J., & Pack, J.D. (1976). Special Points for Brillouin-Zone Integrations. *Physical Review B*, *13*, 5188–5192. DOI: 10.1103/PhysRevB.13.5188
33. He, H. (2020) Metal Oxide Semiconductors and Conductors. *Solution Processed Metal Oxide Thin Films for Electronic Applications*, Elsevier, 7–30.
34. Roessler, D., & Walker, W. (1967). Electronic Spectrum and Ultraviolet Optical Properties of Crystalline MgO. *Physical Review*, *159*, 733. DOI: 10.1103/PhysRev.159.733
35. Gorczyca, I., Wierzbowska, M., Jarosz, D., Domagala, J., Reszka, A., Dang, D.L.S., … & Teisseyre, H. (2020). Rocksalt ZnMgO Alloys for Ultraviolet Applications: Origin of Band-Gap Fluctuations and Direct-Indirect Transitions. *Physical Review B*, *101*, 245202. DOI: 10.1103/PhysRevB.101.245202

sciendo

LATVIAN JOURNAL OF PHYSICS
AND TECHNICAL SCIENCES
2022, N 6

DOI: 10.2478/lpts-2022-0043

# ISOTHERMAL MECHANICAL CYCLING OF SAPONITE–TITANIUM COMPOSITES IN CONDITIONS OF COMPLEX STRESSED STATE

N.M. Huliieva[1,*], V.V. Pasternak[2]

[1] Lutsk National Technical University,
75 Lvivska Str., 43018 Lutsk, UKRAINE
[2] Lesya Ukrainka Volyn National University,
9 Potapova Str., Lutsk 43025, UKRAINE
*e-mail: n.huliieva@lntu.edu.ua

It has been experimentally shown that in the isothermal mechanocycling of continuous cylindrical samples of saponite–titanium composites under conditions of a complex stress state, a reversible deformation of the properties of martensitic inelasticity is observed, which appears during thermal cycling at intervals of martensitic transformations.

According to the results of the experiment, the influence of the ratio between the static and cyclic components of the stress on the change of shear deformation in a complex stress state during mechanical cycling with axial load is estimated.

***Keywords:*** *Complex stress state, cylindrical samples, mechanocycling, orthogonal loading saponite–titanium composites.*

## 1. INTRODUCTION

Details of executive power mechanisms of different functional purposes in mechanical engineering made materials with the effect of shape memory (ESM) [1]. They are usually under the simultaneous influence of axial and tangential stresses. For their manufacture it is necessary to choose metals or alloys that have the appropriate mechanical characteristics and deformation properties of materials at different temperature and force effects [2]. There are a few publications on the mechanical behaviour of composites based on saponite–titanium and other materials with shape memory in a complex stress state today and this suggests the relevance of the research in this area [3].

ESM, the phenomena of martensitic inelasticity, the effects of multiple revers-

ible shape memory, transformation plasticity, reversible shape memory, deformation of oriented transformation, etc. have been widely studied [4]. The above-mentioned phenomena are usually initiated by martensitic reactions associated with thermal cycling of the material. Work on mechanocycling of ESM material in a complex stress state in most cases is devoted to the determination of long-term strength, less often the structure of the material under similar exposure is studied [5]. The authors [6] recorded that during isothermal mechanocycling in the two-phase state, the material was more plastic and less susceptible to equalization of the voltage intensity amplitude. In [7], it was shown that the active deformation of the ESM material in isothermal conditions may be accompanied by phenomena of martensitic inelasticity, similar to those caused by the transformational change in temperature [8]. Therefore, it can be argued that the phenomena of martensitic inelasticity are initiated by isothermal mechanocycling.

This article presents the method of experiment and, in part, the results of systematic research on the study of the deformation behaviour of a material with the effect of shape memory, which is in a complex, stress state under conditions of active deformation at constant temperature.

## 2. MATERIALS AND METHODS

An experimental setup was constructed in the scientific laboratory of Lutsk National Technical University [9], which allows taking readings from the sample separately or simultaneously by stretching or compressing at forces up to 5000 N and torque up to 5 N×m under conditions of change or constant temperature [10].

During the experiment, coaxial fixation was reached by twisting angle of the sample and the axial movement of the end face of the shaft. This allows you to calculate the shear and longitudinal deformation of the sample. Heating was performed using self-propagating high-temperature synthesis [11]. The temperature of the sample during the experiment was recorded using a thermocouple of tungsten rhenium TR5 with a diameter of 100–200 μm [12]. To control the homogeneity of the heating of the sample, two thermocouples used, which were installed at different points.

*Method of determining the axial deformation.* When determining the axial deformation, the instrumental error associated with the thermal effect of the installation was taken into account [13]. In the installation a reference sample made of St.3 was fixed with a well-known coefficient of thermal linear expansion $\alpha = 1.06\times10^{-5}$ $K^{-1}$ and the dilatogram was determined from the compatible thermal effect of the reference sample and installation [14]. From the obtained total dilatogram, dilatogram of the reference sample was determined, highlighting the thermal effect of this installation. Subsequently, the greenhouse effect of the installation was calculated either by adding it to the reversible composition of the strain during stretching and subtraction during compression. The error in the data of axial deformation was ±0.005 %, and the temperature was ±1 K [15].

The experimental setup made it possible for axial deformation to obtain and fix in isothermal conditions significant inelastic axial deformations during torsion and shear [16].

The samples were made of one batch of saponite–titanium composite rods (Table 1)

and had the shape of solid cylindrical rods with a diameter of 5 mm [17]. The length of the working part of the first series was 25 mm, the second – 15 mm, the total length was 55 and 45 mm, respectively. Samples of the second series were used for mechanocycling under conditions of constant or variable compressive force [18].

**Table 1.** Material for Research

| Series of samples | Diameter, mm | Length of a working part, mm | Total length, mm |
|---|---|---|---|
| 1 | 5 | 25 | 55 |
| 2 | 5 | 15 | 45 |

The values of the characteristic temperatures of the phase transitions are given in Table 2. Heat treatment of samples was carried out: annealing at a temperature of 820 K for 30 minutes, cooling in the atmosphere.

**Table 2.** Temperature of Phase Transformations, K

| $M_1$ | $M_2$ | $A_1$ | $A_2$ |
|---|---|---|---|
| 334 | 292 | 382 | 492 |

In the first experimental studies (modes I÷III), the samples were twisted with a constant torque with a static voltage τo, and then mechanocycled with an axial voltage. During the second stage (modes IV÷VII), the samples were stretched or compressed, creating a static stress σ, after which they were mechanocycled by torsion [19]. The samples were subjected to isothermal mechanocycling (Fig. 1) at normal or tangential stresses under pulsation cycles under the action of constant orthogonal deformation. The pulsation period or half-period of symmetry of mechanocycles was 120 s.

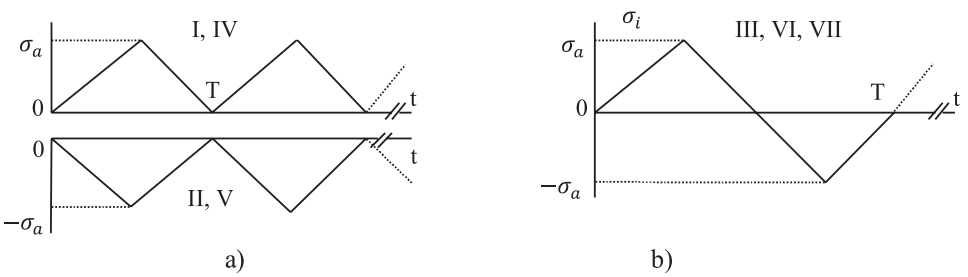


*Fig. 1.* Load modes: a) static: I and II – torsion, IV – axial tensile deformation, V – compression; b) symmetrical: III – torsion, VI – axial tensile deformation, VII – compression.

Stress intensity due to the static component of the stress state $\sigma_i = \sqrt{3}\,\tau_0$ (where $\tau_0$ is the tangential stress that arises due to the action of static load). The maximum intensity due to the cyclic component of the stress state $\frac{\sigma_i}{\sigma_i^{max}}$ (where $\sigma_a$ is the amplitude of cyclic stresses) was taken as 50 MPa, 100 MPa, 150 MPa, 200 MPa for both voltages [20].

The intensity of the DC component of the voltage ($\sigma_i$) from sample to sample was one of the following: 50 MPa, 100 MPa, 150 MPa, 200 MPa. The amplitude of cyclic stresses $\frac{\sigma_i}{\sigma_i^{max}}$ in a particular sample increased every 12–16 mechanocycles and consistently took all the above values [21].

In this case, in each of the studied samples, the ratio $\frac{\sigma_i}{\sigma_i^{max}}$ in relation to the initial ratio changed equally, successively decreased by 2, 3, 4 times. Experimental studies were performed at three different temperatures (Table 3): martensitic $T_M$, biphasic $T_B$ and austenitic state $T_A$ of the samples.

**Table 3.** Temperature for Research, K

| $T_M$ | $T_B$ | $T_A$ |
|---|---|---|
| 320 | 400 | 525 |

The relationship between static loads and amplitudes of cyclic loads are given in Table 4. At each temperature, 16 indicators $K=\frac{\sigma_i}{\sigma_i^{max}}$ were determined. Shear and axial deformations caused by static or alternating cycling stress were recorded [22]. Then one or two mechanocycles were performed without static load in a complex stress state, after which the samples were thermocycled.

**Table 4.** Load

| $K=\frac{\sigma_i}{\sigma_i^{max}}$ | | $\sigma_i^{max}$, MPa | | | |
|---|---|---|---|---|---|
| | | 50 | 100 | 150 | 200 |
| $\sigma_i$, MPa | 50 | 1 | 0.5 | 0.33 | 0.25 |
| | 100 | 2 | 1 | 0.67 | 0.5 |
| | 150 | 3 | 1.5 | 1 | 0.75 |
| | 200 | 4 | 2 | 1.33 | 1 |

## 3. EXPERIMENTAL RESULTS AND DISCUSSION

The main results of experimental research are presented in Figs. 2–5. It is shown that the deformation of one component of the deformation always causes a change in the orthogonal component of the deformation, but for different modes and temperatures of deformation the results are different. Some modes are characterised by curves showing the change in the orthogonal component of the deformation from the number of mechanocycles (Figs. 6–8). In the first mechanocycles for all modes of deformation, as a rule, unilateral deformation of the orthogonal component was observed due to static load. In Modes I and II at the martensitic state (Fig. 6a) during axial mechanocycling there was a reverse deformation in the direction of torque (mechanocyclic creep), which practically stopped until the seventh or eighth cycle. The maximum shear deformations were recorded in the conditions of mechanocycling by stretching at amplitudes $\sigma_i^{max}$ = 200 MPa. Figure 6b shows the dependence of the amount of shear deformation 10 of the cycle on the ratio $\frac{\sigma_i}{\sigma_i^{max}}$. This is due to $\tau_0$ – the magnitude of the static voltage and σ – the amplitude of the pulsating axial voltage. Also, there was a sharp increase in shear deformation with increasing amplitude of normal stress to $\sigma_i^{max}$ = 200 MPa at a constant $\tau_0 = \frac{100}{\sqrt{3}}$ MPa [23]. The greatest deformation occurred at the usual stress of the opposite sign. Both figures show that tension and compression in a complex stress state have different effects on orthogonal deformation under conditions of mechanocycling in the pulsation mode of the cycle [24].

In Mode III of loading (Fig. 5), the sample shows unusual behaviour where after the third cycle deformation "towards force" stops and passes to the phenomenon of mechanocyclic return, i.e., decreases in the general deformation on an orthogonal component from a cycle to a cycle (curve 6 of Fig. 7) [25]. Thus, this phenomenon can be attributed to negative mechanocyclic creep.

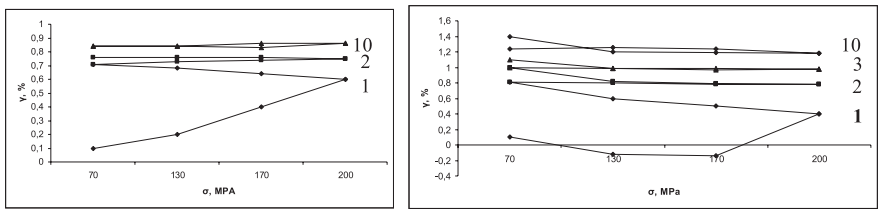


a) b)

*Fig. 2.* The dependence of shear strain on the normal stress σ in static stress mode I and at $\tau_0 = \frac{50}{\sqrt{3}}$ (a), $\frac{200}{\sqrt{3}}$ MPa (b) and T = 290 K. The figures on the graphs correspond to the numbers of mechanocycles.

In Modes I, II, III, VI, VII after reaching a certain number of cycles (N = 6÷10), an inverse change in deformation was observed (curves 10, Figs. 2, 3a, 4, 5), the value of which in some experiments was 0.35 % for one load cycle (curve 10 in Fig. 2b) [26]. At minimum levels of static stresses, as a rule, deformations were recorded toward a fixed stress at the stage of active deformation and its return during unloading of the sample (curves 10 in Figs. 2 and 3) [27]. With the transition to higher levels of static voltages, the results changed. In this case, the active deformation of one of the components of the stress tensor corresponded to the return of deformation to another and, conversely, the unloading of the sample corresponded to the accumulation of deformation toward a given fixed stress (curve 10 in Figs. 2b, 5). Note that most often reversible deformations were observed in Mode III (curve 15 in Fig. 5). In the process of axial mechanocycling under the conditions of a symmetric cycle, typical properties of martensitic inelasticity appeared, such as shape memory effect under active compression (sections of curves 1 – 1'; 2 – 2'; 3 – 3', 15 – 15'); plasticity of direct transformation at the subsequent unloading (sections of curves 1' – 2; 2' – 3; 3' – 3'', 15' – 15''). These phenomena can be considered the effects of martensitic inelasticity, which in this case are initiated by isothermal mechanocycling [28].

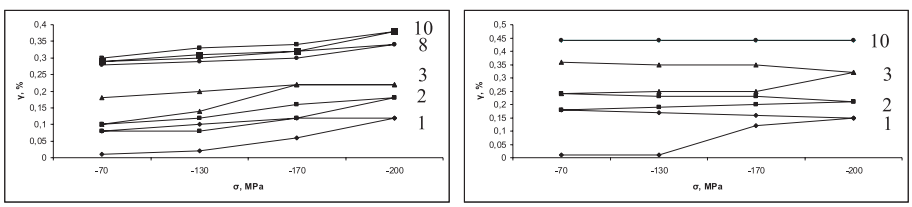


a) b)

*Fig. 3.* Dependence of shear deformation on the ordinary stress σ in Mode II of static stress and at $\tau_0 = \frac{50}{\sqrt{3}}$ (a), $\frac{200}{\sqrt{3}}$ MPa (b) and T = 290 K.

In the analysis of experimental studies of Mode III for the fifth and tenth mechanocycles with increasing amplitude of the normal stress $\sigma_i^{max}$, ($\sigma_i$ = 50, 100, 150, 200 MPa), change of shear deformation depending on the stress ratio $\frac{\sigma_i}{\sigma_i^{max}}$ and temperatures T has three fundamentally different trends: shear deformation increases with the number of cycles; shear deformation in the process of mechanocycling demonstrates a reverse change; shear deformation gradually decreases with the number of cycles [29].

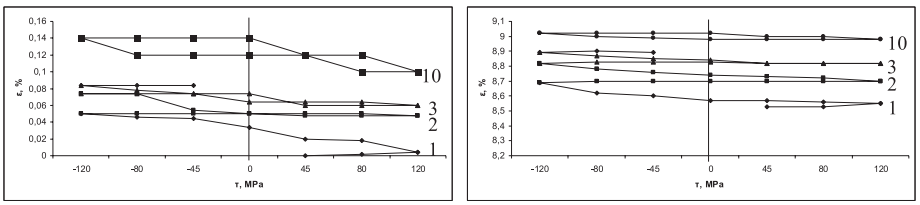


a) b)

*Fig. 4.* The dependence of the axial deformation on the tangential stress during mechanocycling in Mode VI mode, at the tensile stress $\sigma_i$ = 50 MPa (a), 200 MPa (b) and T = 290 K.

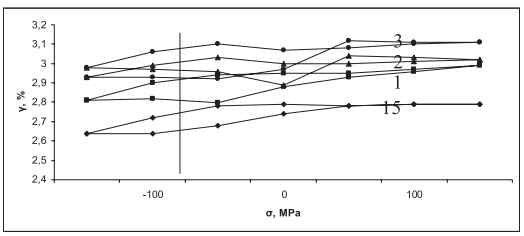


*Fig. 5.* Dependence of shear shift X axis on σ in Stress Mode III, at $\tau_0$ = 115.5 MPa and T = 290 K.

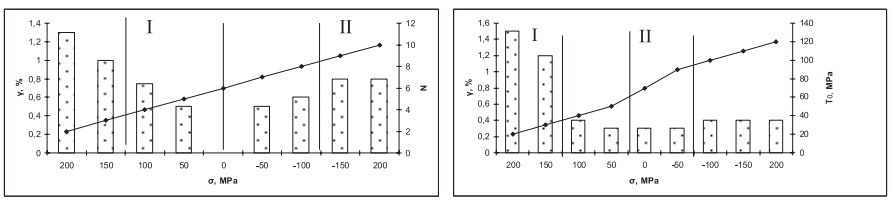


a) b)

*Fig. 6.* Dependences of shear deformation in Modes I, II at T = 290 K: a) on the number of cycles N and the amplitude of mechanocycling σ at $\tau_0 = \frac{200}{\sqrt{3}}$ MPa; b) the magnitude of static voltage and the amplitude of mechanocycling σ γ.

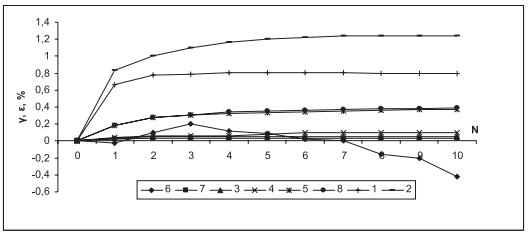


*Fig. 7.* Dependences of shear (1÷6) and axial (7÷8) deformations formed in the process of mechanocycling on the number of cycles for Modes: I (1, 2) at ($\sigma_i$ = 50 MPa and $\sigma_a$ = 200 MPa (1), $\sigma_i$ = 200 MPa and $\sigma_a$ = 200 MPa (2); II (3 ÷ 5) at $\sigma_i$ = 50 MPa and $\sigma_a$ = 100 MPa (3), $\sigma_a$ = 200 MPa (4), $\sigma_i$ = 200 MPa and $\sigma_a$ = 200 MPa (5); III (6) at $\sigma_i$ = 50 MPa and $\sigma_a$ = 150 MPa (6); VI (7, 8) at $\sigma_i$ = 200 MPa and $\sigma_a$ = 50 MPa (7), $\sigma_a$ = 200 MPa (8) at T = 290 K.

Figure 8 presents the dependence of orthogonal shear deformation on the number of cycles with additional and negative axial deformation in Mode III mode under conditions of gradual change of amplitude of normal stress for different relations $K = \frac{\sigma_i}{\sigma_i^{max}}$ between static stress and amplitude of cyclic stress change [30].

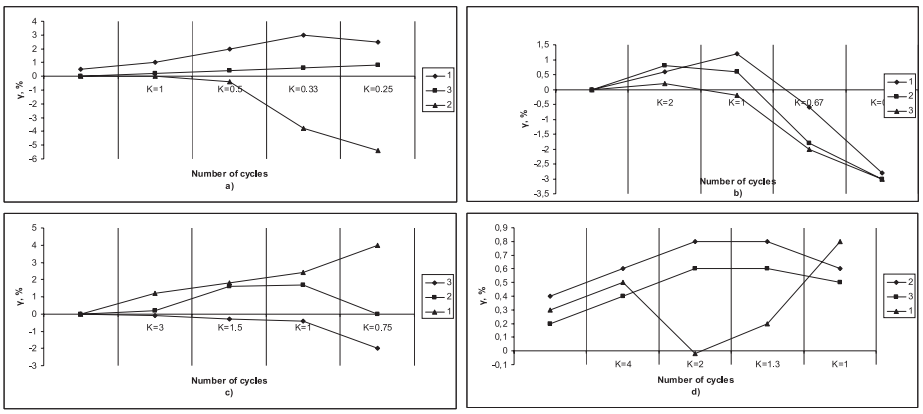


*Fig. 8.* Dependence of shear deformation on the number with additional and negative axial deformation (Mode III) under conditions of gradual change of amplitude of normal stress $\sigma_a$ = 50 (region I), 100 (II), 150 (III), 200 MPa IV) at T = 290 K (1), 370 K (2), 510 K (3), for the values $\sigma_i$ = 50 (a), 100 (b), 150 (c), 200 MPa (d).

At the lowest $\sigma_i$ = 50 MPa (Fig. 8), the value of the mechanocyclic return reaches the maximum value at a temperature corresponding to the two-phase state (curve 2a). At $\sigma_i$ = 100 MPa (Fig. 8b), there is the same, almost synchronous, increase, and then the shear deformation decreases at all temperatures, i.e., the sample with increasing amplitude of the axial stress of "untwisting". For $\sigma_i$ = 150 MPa (Fig. 8c) in the martensitic state (curve 1c) with increasing number of mechanocycles shear deformation accumulated in the direction of constant tangential stress increases. At a temperature of 370 K after some increase in deformation, there is a negative mechanocyclic creep. It leads to the initial level of shear deformation at higher values of $\sigma_i^{max}$ = 200 MPa. At a temperature corresponding to the austenitic state of the sample, a gradual mechanocyclic return is observed. For all temperatures at $\sigma_i$ = 200 MPa (Fig. 8d), slight changes in shear deformation are observed [31].

Therefore, according to the results of experimental data, in the martensitic state it is impossible to unambiguously determine the change in the deformation shift (its increase or decrease) in the process of mechanocycling along the axial stress component, i.e., there is no necessary dependence on the parameter $K = \frac{\sigma_i}{\sigma_i^{max}}$. In the two-phase state, the orthogonal component of the deformation increases only when K > 1, i.e., the sample "twists" in the direction of static torque; in the case of K ≤ 1 the sample begins to "untwist". In the austenitic state, it is impossible to unambiguously link the change in shear deformation with the parameter K; however, it can be noted that it practically does not change at the minimum and maximum values of $\sigma_i$, namely, at 50 and 200 MPa [32].

Analysing all experimental data on isothermal mechanocycling of continuous cylindrical samples of saponite–titanium composites in Mode III in the martensitic state, in 56 % of cases of different ratios $K = \frac{\sigma_i}{\sigma_i^{max}}$ there is only an increase in shear deformation, i.e., an increase towards constant torque. Mechanocyclic return is mainly

observed after 5–7 cycles, and provided that the intensity of the static and dynamic components of the loads at K = 1. It is observed that in the two-phase state at K > 1 there is only accumulation of deformation, and at K ≤ 1 only return of deformation (during the first stage of 5–7 cycles, in the second and subsequent with the first mechanocycle). In the austenitic state, either accumulation of deformation (54 % of cases) or return from the first mechanocycle was detected. At the amplitude of cyclic stresses $\sigma_a$ = 50 MPa at all temperatures in 85 % of all experiments there is an accumulation of shear component deformation.

## 4. CONCLUSIONS

In the study of isothermal cycling of saponite–titanium composites under conditions of complex stress state, the martensitic stress has a number of factors. The first is mechanocyclic creep, which usually leads to irreversible accumulated deformation towards a fixed stress. This may be due to the texturing of the material in the process of mechanical cycling, as well as the evolution of oriented and undirected internal microvoltages. As the cycles are repeated, there is a mechanical slander, which significantly reduces the intensity of deformation accumulation and leads to its saturation. The second factor is along with the irreversible deformation of mechanocycling. According to the Clausius-Clapeyron ratio, it can be accompanied by direct and inverse martensitic reactions and lead to reversible deformation of the material. This also applies to Modes IV and V, as well as some schemes of Loaded Mode II. Of greatest interest is the case when, along with the reversible deformation in the process of mechanocycling, there is a mechanocyclic return of the orthogonal component of the deformation or a negative mechanocyclic creep. This phenomenon is obviously due to the fact that at the initial stage of the mechanocycle there is an accumulation of irreversible deformation, which is realised more due to the channels of martensitic inelasticity. After a certain number of cycles, irreversible complex deformations occur. It is almost completely neutralized due to mechanical hardening, as a result of which the restoration of deformation from cycle to cycle begins to appear.

Analysing the results of research, we can draw the following conclusions:

The mechanocycle on one component of deformation always causes change of orthogonal deformations. In the first cycles, in all load modes, there is a gradual accumulation towards the load.

With the accumulation of a certain number of cycles there is an inverse deformation or complete independence of the deformation from the number of cycles.

The strongest effect of reversible deformation is manifested in Mode III, if the cycling is carried out in a symmetrical cycle "stretching – unloading – compression – unloading".

Mode III is characterised by the phenomenon of return mechanocycling, which has the largest value at small values of $\tau_0$ = 50 MPa at a temperature corresponding to the two-phase state.

Different influence on the shear of half-compression and tensile deformation is recorded. In the two-phase state with increasing number of cycles the semi-cycle of compression has a predominant effect on shear deformation and in this state at $\frac{\sigma_i}{\sigma_i^{max}} = 1$ there is a clear change of sign with increasing shear deformation. In the austenitic

state, the semi-cycle of stretching has the predominant effect. In the martensitic state during semi-stretching and compression, changes do not occur.

Therefore, some of these phenomena can be explained by the presence of martensitic reactions that occur during mechanocycling [3].

## REFERENCES


1. Yuan, H., Fauroux, J.–Ch., Chapelle, F., & Balandraud, X. (2017). A Review of Rotary Actuators Based on Shape Memory Alloys. *Journal of Intelligent Material Systems and Structures, 28* (14), 1863–1885, DOI: org/10.1177/1045389X16682848
2. Lavakumar, A. (2017). Mechanical Properties of Materials. *Concepts in Physical Metallurgy, 4,* 5–22. https://doi.org/10.1088/978-1-6817-4473-5ch5
3. Huliieva, N. M., Somov, D. O., Pasternak, V. V., Samchuk L. M., & Chetverzhuk, T. I. (2020). The Selection of Boron Nitride Circles for Grinding Saponite – Titanium Composites Using Non-Parametric Method. *Latvian Journal of Physics and Technical Sciences, 57* (6), 68–77. DOI: 10.2478/lpts-2020-0033
4. Tahara, M., Kim, H. Yo., Hosoda, H., & Miyazaki, Sh. (2009). Shape Memory Effect and Cyclic Deformation Behavior of Ti–Nb–N Alloys. *Functional Materials Letters, 2* (2), 79–82. DOI: org/10.1142/S1793604709000600
5. Sun, Q., Cao, B., Iwamoto, T., & Suo, T. (2021). Effect of Impact Deformation on Shape Recovery Behavior in Fe-Mn-Si Shape Memory Alloy under Shape Memory Training Process with Cyclic Thermo-Mechanical Loading. *Science China Technological Sciences.* DOI: org/10.1007/s11431-020-1759-y
6. Zabolotnyi, O., Pasternak, V., Ilchuk, N., Huliieva, N., & Cagáňová, D. (2021). Powder technology and software tools for microstructure control of $AlCu_2$ samples. In: *Proceedings of the 4th Int. Conf. on Design, Simulation and Manufacturing: The Innovation Exchange, DSMIE-2021* (pp. 585–593), 8–11 June 2021. Lviv, Ukraine: Manufacturing and Materials Engineering: Springer.
7. Ohki, T., Ni, Q.-Q., Ohsako, N., & Iwamoto, M. (2004). Mechanical and Shape Memory Behavior of Composites with Shape Memory Polymer. *Composites Part A: Applied Science and Manufacturing*, *35* (9), 1065–1073. DOI:org/10.1016/j.compositesa.2004.03.001
8. Murasawa, G., Tohgo, K., & Ishii, H. (2004). Deformation Behavior of NiTi / Polymer Shape Memory Alloy Composites – Experimental Verifications. *Journal of Composite Materials, 38* (5), 399–416. DOI: org/10.1177/0021998304040553
9. Turov, V., Tryasuchev, L., Klochko, V., & Zvonytsky V. (2008). IPC Tensile Testing Device. N 33345. *Database of Patents of Ukraine.* Available at https://uapatents.com/3-33345-pristrijj-dlya-viprobuvannya-na-roztyag-stisk.html
10. Sheldon, B.W., Rajamani, A., Bhandari, A., Chason, E., Hong, S.K., & Beresford, R. (2005). Competition between Tensile and Compressive Stress Mechanisms during Volmer-Weber Growth of Aluminum Nitride Films. *Journal of Applied Physics, 98,* 043509. DOI:org/10.1063/1.1994944
11. Patent of Ukraine 91287, IPC B22F 3/23 (2006.01) C01G 1/00 (2014.01). Reactor for Self-propagating High-Temperature Synthesis (SHS process). L. Samchuk, N. Guliyeva, V. Rud, O. Povstyanoy, I. Savyuk, Yu. Vorobey, M. Zaikin. Lutsk National Technical University, Lutsk, 25.06.14, 12.
12. Rud, V., Samchuk, L., & Guliieva, N. (2014). Application of Pyrometric Technique for Imaging of Front SHS Burning. *Bulletin of Vinnytsia Polytechnic Institute: Mechanical Engineering and Transport. Vinnitsa, 6,* 97–101.
13. Shmyg, R., Boyarchuk, V., Dobryansky, I., Barabash V., & Schmig, R.A. (2010). Measurement Error. *Terminological Dictionary-Reference Book on Construction and Architecture*. Lviv, 159.

14. Standard. (2017). *ISO 12106:2017.* Metallic Materials. Fatigue Testing. Axial-Strain-Controlled Method, 38.
15. Anwar, N., & Najam, F. (2017). Chapter Three – Axial-Flexual Response of Cross-Sections. *Structural Cross Sections Analysis and Design*, 137–249.
16. Huliieva, N. (2019). Exposure to Saponite-Titanium Composite with Subsequent Deformation of Intense Plastic Torsional Deformation. *Abstracts of the VI Scientific Conference Nanoscale Systems: Structure, Properties, Technologies* (pp. 3–6), Kyiv: NANSIS 2019.
17. Huliieva, N., Pasternak, V., & Samchuk, L. (2020). Application of deep sanding method of saponite – titanium blanks. In: *VI International Scientific and Practical Conference Scientific Achievements of Modern Society* (p. 119), 5–7 February 2020. Liverpool: UK.
18. Sheremetyev, V., Prokoshkin, S., Brailovski, V., & Dubinskiy, S. (2015). Investigation of the Structure Stability and Superelastic Behavior of Thermomechanically Treated Ti-Nb-Zr and Ti-Nb-Ta Shape-Memory Alloys. *The Physics of Metals and Metallography, 116* (4), 413–422. DOI: 10.1134/S0031918X15040158
19. Ropyak, L., & Velichkovych, A. (2016). *Investigation of the Stress State of a Multifunctional Coating during Stretching or Torsion.* Kyiv: KPI them. Igor Sikorsky, 194–196.
20. Gomatam, R., & Sancaktar, E. (2006). The Effects of Stress State, Loading Frequency and Cyclic Waveforms on the Fatigue Behavior of Silver-Filled Electronically-Conductive Adhesive Joints. *January Journal of Adhesion Science and Technology, 20* (1), 53–68. DOI: 10.1163/156856106775212378.
21. Ma, Z., Zhao, H., & Liu, Ch. (2021). Prediction Method of Low Cyclic Stress-Strain Curve of Structural Materials. *Materials Transactions, 56* (7), 1067–1071. DOI: 10.2320/matertrans.M2015085]
22. Gooch, Ja. (2011). Cyclic Stress Strain. *Encyclopedic Dictionary of Polymers*, 189–189. DOI: 10.1007/978-1-4419-6247-8_3235
23. Kelly, Ja. (2017). Shear Deformation and the Buckling of Columns, Revisited. *Civil Eng Res J. 2* (1), 555579. DOI:10.19080/CERJ.2017.02.555579
24. Herrmann, H., & Bucksch, H. (1991). Shear deformation. *Dictionary Geotechnical Engineering/Wörterbuch GeoTechnik,* 2633–3379. Springer, Berlin, Heidelberg. DOI: 10.1007/978-3-642-41714-6_192792
25. Bhaskar, K., & Varadan, T. (2021). Shear Deformation Theories (pp. 181–195). In: *Plates*. Springer, Cham. DOI: org/10.1007/978-3-030-69424-1_11
26. Casati, R., Vedani, M., & Tuissi A. (2014). Thermal Cycling of Stress-Induced Martensite for High-Performance Shape Memory Effect. *Scripta Materialia*, *80*, 13–16. DOI:10.1016/j.scriptamat.2014.02.003
27. Lázpita, P., Villa, E., Villa, F., & Chernenko, V. (2021). Temperature Dependent Stress–Strain Behavior and Martensite Stabilization in Magnetic Shape Memory $Ni_{51.1}Fe_{16.4}Ga_{26.3}Co_{6.2}$. *Single Crystal Metals*, *11*, 920. DOI: org/10.3390/met11060920
28. Müllner, P., Chernenko, V., & Kostorz, G. (2004). Large Cyclic Magnetic-Field-Induced Deformation in Orthorhombic (14M) Ni–Mn–Ga Martensite. *J. Appl. Phys, 95*, 1531–1536.
29. Pagounis, E., & Muellner, P. (2018). Materials and actuator solutions for advanced magnetic shape memory devices. In: Proceedings of the ACTUATOR 2018, 16th International Conference on New Actuators (pp. 1–7), 25–27 June 2018. Bremen, Germany.
30. Kustov, S., Pons, J., Cesari, E., & Van Humbeeck, J. (2004). Chemical and Mechanical Stabilization of Martensite. *Acta Mater, 52*, 4547–4559.
31. Samy, N., Daróczi, L., Tóth, L., Panchenko, E., Chumlyakov, Y., Surikov, N., & Beke, D. (2020). Effect of Stress-Induced Martensite Stabilization on Acoustic Emission Characteristics and the Entropy of Martensitic Transformation in Shape Memory $Ni_{51}Fe_{18}Ga_{27}Co_4$ Single Crystal. *Metals*, *10*, 534.
32. Roytburd, A. (2000). Intrinsic Hysteresis of Superelastic Deformation. *Mater. Sci. Forum*, 389–392.

sciendo

LATVIAN JOURNAL OF PHYSICS
AND TECHNICAL SCIENCES
2022, N 6

DOI: 10.2478/lpts-2022-0044

# COMPLEX TYPE II SOLAR RADIO EVENT ON 4 JULY 2022

J. Kallunki

Aalto University,
Metsähovi Radio Observatory, Finland
*e-mail: juha.kallunki@aalto.fi

On 4 July 2022, a complex low-frequency solar radio burst was observed in Metsähovi Radio Observatory of Aalto University. The radio burst was observed at a frequency range between 20 and 80 MHz. In GOES (Geostationary Operational Environmental Satellite) class, the event was classified as C5.1. However, coronal mass ejection (CME) was not associated to this event. The observed radio burst was a long-lasting (~10 minutes) event, and it could be mainly classified as type II solar radio event. Also type III solar events were observed before long-lasting type II event. The event includes common frequency drifting emission structures, both fundamental and harmonic structures, but also rarely observed continuum-like or stationary structure. It is assumed that the continuum-like radio emission structure is originated from the stationary flare (coronal) loop, which was visible over the whole event. The drifting emission structure means accelerated electrons, which are produced by the shock related phenomena. The paper provides the observations from this event on radio wavelength, and also soft-X-ray regime and optical wavelength (AIA 171). In addition, a possible, simplified scenario is presented for forming the drifting and continuum solar radio emissions in type II solar burst.

***Keywords:*** *Radio astronomy, solar activity, solar radio emission, type II solar radio burst.*

## 1. INTRODUCTION

Low-frequency (< 100 MHz) solar radio bursts have been studied for decades. They have a major role in the space weather investigations since they originate in the same layers of the solar atmosphere in which geo-effective disturbances originate [1]. The radio bursts can be classified based on how they appear in dynamic spectrum, e.g., based on their duration and frequency drift. The most common types of radio bursts are: I, II, III, IV and V. Other more complex bursts are also possible, which are not matching directly with I–IV classifications. Type II solar radio bursts have long been linked to solar eruptive events such as coronal mass ejections (CMEs), also they have been linked to the flare blast shock waves. Type II solar radio emission often occurs after the lift-off of the CME [2]. It has also been reported that emission steps of type II radio burst are the following: (1) the acceleration of electrons by the shock, (2) the excitation of Langmuir waves by the energetic electrons by streaming instabilities, and (3) the conversion of Langmuir waves into escaping radiation at the fundamental (*F*) and second harmonic (*H*) of the electron plasma frequency ($f_{pe}$) [3]. Both drifting and continuum-like emission structures have been detected in touch with type II bursts. The drifting structures are related to moving shocks. The stationary emission is forming at the stage when the CME causes the streamer to expand quickly locally [4]. In addition, type II solar radio bursts typically occur at around the time of the soft X–ray peak [1]. Solar type III radio bursts result from impulsively accelerated electrons. Their radio emission is drifting fast from higher to lower frequencies [4], [5].

Type II solar radio bursts, which have a continuum-like or stationary emission structure, have been reported earlier, e.g., [6]–[8]. However, these events are not very common. Most of the type II radio events have a drifting emission structure. Previously reported events have had clear relation to CMEs. However, this event had not any connection to CME. This article presents and analyses a complex low-frequency solar radio event, which has both drifting and continuum-like emission structures. The complex low-frequency (<100 MHz) solar radio event was observed on 4 July 2022. The radio observations were made at Metsähovi Radio Observatory (MRO) of Aalto University.

## 2. INSTRUMENTATION

Metsähovi Radio Observatory (MRO) of Aalto University, located in southern Finland (GPS coordinates: N 60:13.04, E 24:23.35), installed a crossed-dipole antenna (CDA) manufactured by Reeve Observatory in October 2017. The new antenna, dubbed the Metsähovi Solar Observing Low-frequency Antenna METSOLA, has frequency coverage between 18 MHz and 90 MHz. The antenna has two different polarization outputs (east–west and north–south), which makes it possible to study also the polarization properties of solar flares. The Sun is rather vactive at frequencies below 100 MHz even if the solar activity phase is low. On the other hand, one of the main challenges when making radio astronomical observations on lower fre-

quencies ($f \simeq 100$ MHz) is radio frequency interference (RFI). This frequency range is allocated for various services such as broadcasting, amateur and mobile. However, it has been found that the observing band between approximately 30 and 80 MHz was still reasonably free from interferences and usable for solar observations [9], [10]. Figure 1 shows METSOLA instrument.

In 2021, the noise calibration was added to the system (east–west polarization). This makes it possible to estimate the flux density of the observed radio bursts. The flux density estimation method is described more carefully in [11]. In this study, the time and frequency profiles of the observed solar radio burst were studied; thus, there was no need for the accurate flux calibration.

*Fig. 1.* METSOLA instrument installed in Metsähovi Radio Observatory of Aalto University.

## 3. OVERVIEW OF OBSERVATIONS

On 4 June 2022, a complex solar type II radio burst was observed, starting at 13:35 UT, which had both drifting and stationary or continuum-like structures, which was preceded by type III solar event (starting at 13:34 UT). The event was observed at a frequency range between 20 and 85 MHz. The radio data were obtained with the radio telescopes of Metsähovi Radio Observatory of Aalto University. In GOES class, the event was classified as C5.1. However, CME was not associated to this event. Near the soft-X-ray peak (0.1–0.8 nm), type III solar burst was detected. The soft-X-ray peak was at 13:31 UT (0.05-0.4 nm) and 13:33 UT (0.1–0.8 nm), marked with a red dashed line in Fig. 2.

Type II solar radio burst started (~13:34:20 UT) with the drifting structure; both fundamental (F) and harmonic (H) emissions could be detected. A minute after that, stationary or continuum-like emission structure was starting (at 13:35:30 UT) at frequencies between ~45 and 48 MHz, marked with a green dashed line in Fig. 1. The stationary emission went until 13:41 UT, which was followed by three different drifting structures (type II solar burst). The event was recorded with two different polarizations (east–west and north–south) using METSOLA instrument. No significant differences in measurements between the linear polarizations were noted in this case. Figure 2 shows the dynamic spectra of the observed low-frequency solar radio event.

Figure 3 shows the GOES soft-X-ray flux on this event. The soft-X-ray flux peaked (0.1–0.8 nm) about one minute before the first type III solar burst. Figure 4 presents the solar radio map at 37 GHz, which was observed around after two hours when the event started. The radio map was observed with MRO 14-metre radio telescope. An area marked with a blue arrow shows the active regions, which produced the radio burst presented here. The maximum radio brightness intensity is 105.75 % of the QSL (8570 K).

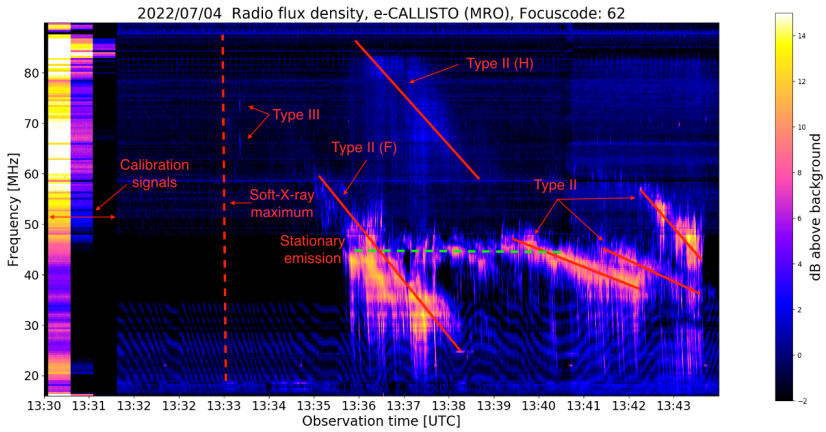


*Fig. 2.* A complex low-frequency (20–90 MHz) solar event observed on 4 June 2022.
A wavy signal, which is observed over the whole-time range, is a sign of RFI (Radio Frequency Interference).

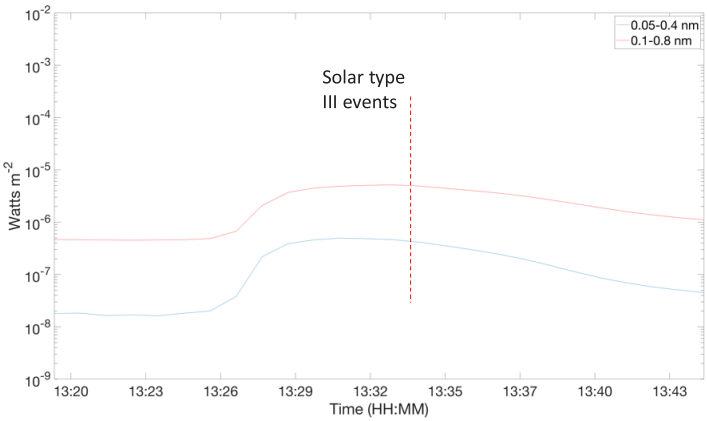


*Fig. 3.* The soft-X-ray flux in the period of the solar radio event. The soft-X-ray event peaks close (approximately with a one-minute difference) to first type III solar burst. The red dashed line indicates the starting time of type III solar burst.

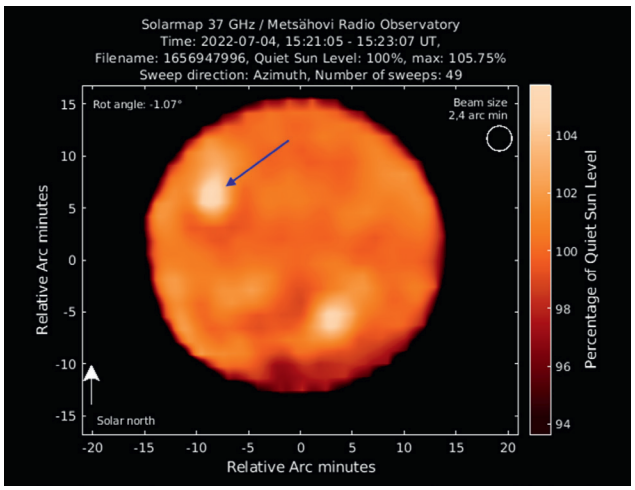


*Fig. 4.* The radio map at 37 GHz, observed at 15:21:05 UT. The blue arrow shows a region, which was an origin of complex solar burst. The map was observed roughly after two hours after the burst occurred.

The observed solar radio map also indicates the fact that the event was relatively weak; thus, the brightness temperature of the active region after two hours from the event was already rather low (105.75 % of the QSL).

In addition, Figure 4 shows SDO/AIA 171 Å seven maps over the radio event occurring period. This wavelength, 171 Å, shows the quiet corona and coronal loops. A larger active region stays stabile over the radio event. However, some smaller flaring region, marked with a red arrow, is visible. This region is located closer to the footpoint of the coronal loop. This flaring region was visible at ~13:32:30 UT, when soft-X-ray peaked. In addition, the flaring region was visible between 13:36:45 UT and 13:42:45 UT. The size of this smaller flaring region was as the largest at 13:36:45 UT. At 13:42:45 UT, the region was barely visible anymore. The coronal (flare) loops were visible over the whole period, and they were rather stable.

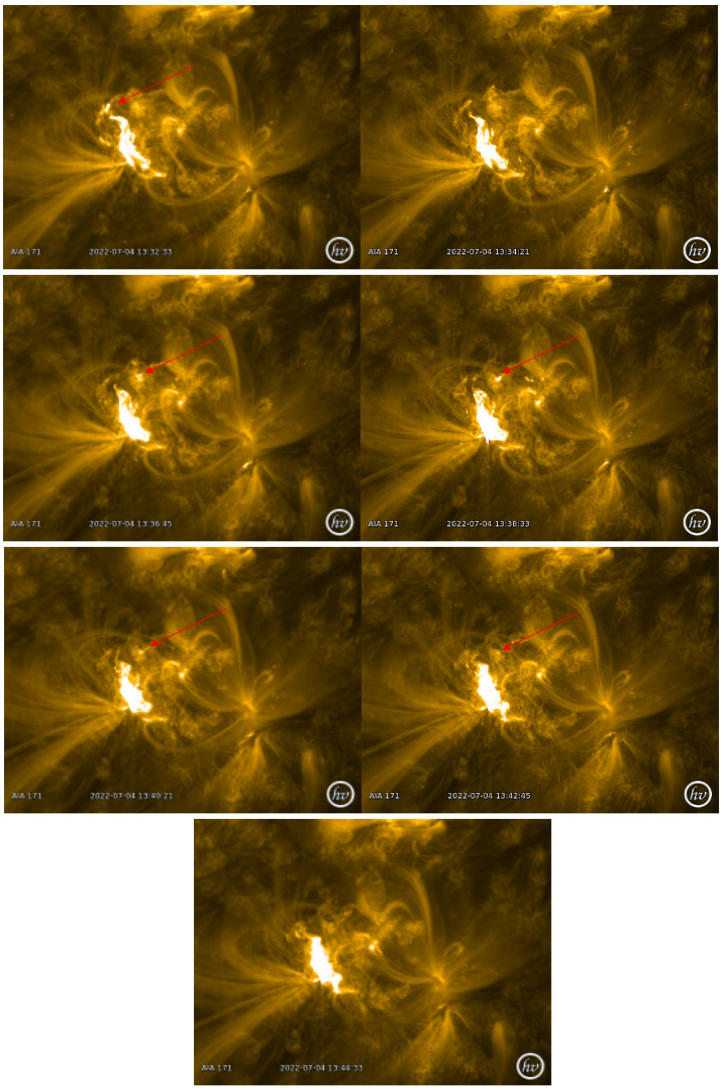

*Fig. 5.* Seven SDO/AIA (171 Å) maps, which show the variation of the flaring region. Red arrows show the location of a smaller flaring region in the footpoint of the flare loop.

### a. Drift Rates of Radio Bursts

The drifting rate ($D$) was defined for each burst structure, according to Eq. (1). The upper observing range of the instrument is 90 MHz; thus, the upper frequency band of harmonic type II solar burst could not be observed. Besides, the real upper observing limit was 85 MHz due to prevailing RFI environment.

$$D = \frac{df}{dt} = \frac{f_1 - f_0}{t_1 - t_0}, \quad (1)$$

where $f_0$ and $f_1$ are the frequency of the burst at start ($t_0$) and end ($t_1$) of the observed burst, respectively. Table 1 presents the drift rates for each burst structure. In Table 1, $F$ indicates fundamental structure and $H$ fundamental structure, respectively.

**Table 1. The Drift Rates for Each Burst Structure**

| Starting time (UT) | Drift rate (MHz $s^{-1}$) | Burst type |
|---|---|---|
| 13:34:20 | -2.89 | Type III |
| 13:36:00 | -0.17 | Type II (F) |
| 13:36:50 | -0.16 | Type II (H) |
| 13:38:58 | -0.08 | Type II |
| 13:40:13 | -0.06 | Type II |
| 13:43:16 | -0.17 | Type II |

After continuum structure, three drifting structures were followed. The drift rate of two first bursts was smaller than the third one. The drift rate of the third burst was consistent with the first type II solar burst. The result was consistent with earlier observation, e.g., [12], [13], where the observed drift rates varied between 0.44 MHz/s and 12 MHz/s for type III solar bursts, and for type II burst frequency drift was at the rate of ~0.14 MHz $s^{-1}$ [4], respectively. It can be conclude that the observed drift rates match accurately with those previously reported. The propagation height of the continuum emission can also be estimated using the Newkirk 1st-order atmospheric density model, e.g., [9].

$$n_e = n_0 \times 10^{4.32\frac{R_\odot}{R}}, \quad (2)$$

where $R$ is distance from the solar centre, $R_\odot$ is the solar radius, $n_0$ is $4.2 \times 10^4$ $cm^{-1}$ and $n_e$ is electron density on certain height on the solar atmosphere. The connection between the plasma frequency ($v_{pe}$) and the electron density ($n_e$) can be estimated as follows [e.g., 14]:

$$v_{pe} \approx 9000 \times \sqrt{n_e}. \quad (3)$$

Frequencies 45 and 48 MHz correspond to propagation distances 1.52 $R_\odot$ and 1.55 $R_\odot$, respectively.

## 4. CONCLUSIONS

Type II solar burst with stationary emission structure has been rarely reported. A majority of type II solar events are drifting structures. The prevailing interpretation is that stationary emission is a signature of the standing shock. Associated with type II solar bursts, the so-called herringbone radio burst are also reported [4]. The herringbone

bursts look like a continuum emission, but they have narrow bandwidth and very rapid frequency drift rate [15].

A jet eruption caused a steamer-puff CME, which produced both the stationary and drifting emission structures in connection with type II solar burst [4]. However, in our case, CME was not detected. In addition, it has been reported that type IV burst or continuum radiation is produced by electrons trapped in stationary or slowly moving coronal loops [2]. SDO/AIA 171 Å maps showed clear stationary coronal (flare) loop structures, which were stable over the whole observing period. Our observations support interpretation that the continuum type II radio emission can also be originated from stationary or slowly moving coronal (flare) loops. The drifting emission comes from the moving plasmoid ejection (e.g., filament), which was also detected in SDO/AIA 171 Å maps (Fig. 5). Figure 6 presents a possible scenario for forming the drifting and continuum solar radio emissions on type II solar radio burst, which has been analysed in this study.

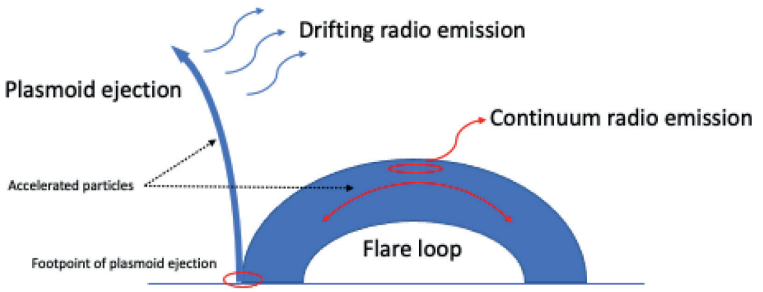


*Fig. 6.* The proposed, simplified scenario for the formation of the drifting and continuum solar radio emissions in type II solar burst. The drifting radio emission comes from the moving structure and continuum emission comes from flare loop, respectively. It can also be assumed that the radio emission comes from the top of the flare loop.

The drifting structure means that the structure is moving in the solar atmosphere (away from the Sun). The radio emission must be the origin from the structure which is moving. This can mean that emission comes from moving plasmoid ejection. The continuum radio emission means that the structure is not moving in the solar atmosphere. It can then be assumed that emission comes from the flare loop, and more precisely from the top of the flaring loop, since the structure is not moving in the solar atmosphere.

As it has been mentioned, events presented here are very unusual and rare. The model presented in Fig. 6 should be confirmed with other similar events. They will be needed to confirm the findings of the present study. The solar activity is rising constantly, and the maximum of Solar Cycle 25 will reach within the next 2–3 years. This will foretell the rising number of active events, and, hopefully, similar events can be observed within this time frame.

## ACKNOWLEDGEMENTS

The HMI data is courtesy of NASA/SDO and the AIA, EVE, and HMI science teams.

## REFERENCES


1. White, S. M. (2007). Solar Radio Bursts and Space Weather. *Asian Journal of Physics, 16*, 189–207.
2. Dulk, G. (2001). Solar Radio Emissions. *Planetary Radio Emissions*.
3. Thejappa, G., Zlobec, P., & MacDowall, R. J. (2003). Polarization and Fragmentation of Solar Type II Radio Bursts. *The Astrophysical Journal, 592* (2), 1234–1240. doi:10.1086/375859.
4. Ergun, R. E. (1998). Wind Spacecraft Observations of Solar Impulsive Electron Events Associated with Solar Type III Radio Bursts. *The Astrophysical Journal, 503* (1), 435–445. doi:10.1086/305954.
5. Reid, H. A. S., & Ratcliffe, H. (2014). A Review of Solar Type III Radio Bursts. *Research in Astronomy and Astrophysics, 14* (7), 773–804. doi:10.1088/1674-4527/14/7/003.
6. Chrysaphi, N., Reid, H. A. S., & Kontar, E. P. (2020). First Observation of a Type II Solar Radio Burst Transitioning between a Stationary and Drifting State. *The Astrophysical Journal, 893* (2). doi:10.3847/1538-4357/ab80c1.
7. Aurass, H., & Mann, G. (2004). Radio Observation of Electron Acceleration at Solar Flare Reconnection Outflow Termination Shocks. *The Astrophysical Journal, 615* (1), 526–530. doi:10.1086/424374.
8. Aurass, H., Vršnak, B., & Mann, G. (2002). Shock-Excited Radio Burst from Reconnection Outflow Jet? *Astronomy and Astrophysics, 384*, 273–281. doi:10.1051/0004-6361:20011735.
9. Kallunki, J., McKay, D., & Tornikoski, M. (2021). First Type III Solar Radio Bursts of Solar Cycle 25. *Solar Physics, 296* (4). doi:10.1007/s11207-021-01790-9.
10. Kallunki, J. (2018). Solar Observing System for Radio Frequencies 5–120 MHz. *Astronomische Nachrichten, 339* (656), 656–660. doi:10.1002/asna.201913545.
11. Kallunki, J., Monstein, C., Kirves, P., Tammi, J., & Mujunen, A. (2022). Calibration of CALLISTO data. *Aalto University publication series Science + Technology, 1/2022*. Available at http://urn.fi/URN:ISBN:978-952-64-0795-1
12. Melnik, V. N. (2015). Decameter Type III Bursts with Changing Frequency Drift-Rate Signs. *Solar Physics, (290)* 1, 193–203. doi:10.1007/s11207-014-0577-8.
13. Li, B., Cairns, I. H., & Robinson, P. A. (2011). Effects of Spatial Variations in Electron and Ion Temperatures on Coronal Type III Bursts. *The Astrophysical Journal, 730* (1).
14. Pohjolainen, S., van Driel-Gesztelyi, L., Culhane, J. L., Manoharan, P. K., & Elliott, H. A. (2007). CME Propagation Characteristics from Radio Observations. *Solar Physics, 244* (1–2), 167–188. doi:10.1007/s11207-007-9006-6.
15. Armatas, S. (2019). Detection of Spike-Like Structures Near the Front of Type-II Bursts. *Astronomy and Astrophysics, 624*, A76. doi:10.1051/0004-6361/201834982.

sciendo

LATVIAN JOURNAL OF PHYSICS
AND TECHNICAL SCIENCES
2022, N 6

DOI: 10.2478/lpts-2022-0045

# ENERGY PERFORMANCE ASPECTS OF NON-RESIDENTIAL BUILDINGS IN LATVIA

A. Kundziņa[1], I. Geipele[1*], S. Lapuke[1], M. Auders[2]

[1]Riga Technical University,
Institute of Civil Engineering and Real Estate Economics
6 Kalnciema Str., Riga, LV-1048, LATVIA
[2]Ministry of Economics of the Republic of Latvia,
Department of Housing Policy
55 Brīvības Str., Riga, LV-1519, LATVIA
*e-mail: Ineta.Geipele@rtu.lv

Increase of energy efficiency is Latvia's national priority and policy instrument that allows reducing consumption of energy and costs, increasing the safety level of energy supply and reducing dependence on import. One of the trends for reducing energy consumption is to increase energy performance of buildings. In compliance with the EU and Latvian political statements, it is required to promote renovation of residential and non-residential buildings.

Studies regarding energy performance aspects in the sector of non-residential buildings in Latvia are comparatively rare; however, non-residential buildings form a considerable part of the building stock, and the increase of their energy performance can bring a significant contribution in achieving the national targets.

The research analyses the sector of non-residential buildings, their characteristic statistical data, energy consumption and requirements of energy performance standards. To characterise this sector more comprehensively, information on energy performance certificates of buildings issued during the period from 2016 to 2021 has been evaluated, allowing to make general conclusions on the energy performance level of different non-residential buildings and provide proposals for trends to increase their energy efficiency.

***Keywords:*** *Building energy performance class and index, energy efficiency, energy performance certificate, non-residential buildings.*

## 1. INTRODUCTION

Latvian policy planning documents set the increase of energy efficiency as a national priority. The Strategy of Latvia for the Achievement of Climate Neutrality by 2050 stipulates that one of the potential solutions for ensuring low carbon development is comprehensive energy efficiency – Increasing of energy efficiency and implementation of the horizontal principle "energy efficiency first" is one of the main factors of sustainable energy sector in Latvia as it reduces the demand for energy generation in different sectors of national economy, as well as in households [1].

In accordance with the EU Directive on the energy performance of buildings [2], [3] and the Regulation (EU) on the Governance of the Energy Union and Climate Action [4], Latvia, as the EU Member State, has to promote renovation of residential and non-residential building stock (both public and private) in order to become highly energy efficient and decarbonised by 2050, promoting the cost-effective transformation of the current buildings into almost zero-energy buildings [5].

The Latvian Energy Policy stipulates that energy efficiency is one of the main tools of the Policy that allows reducing costs and, with reduction of energy consumption, increases the safety level of energy supply and reduces dependence on import. These aspects have become especially topical during the past year. Latvian laws and regulations include the requirements to ensure rational usage and management of energy resources to achieve sustainable national economy. Latvian mandatory national target in the field of energy efficiency for the period of 2021–2030 is a cumulative end-use energy savings of 73.72 PJ (20472 GWh or 1.76 Mtoe) [6]. To reach the set savings target at households, as well as in commercial and public [7] sectors, about a half of the planned savings of energy consumption is planned to be achieved by increasing energy performance of buildings (residential, public, including state administration, and commercial sector buildings).

Studies regarding energy performance aspects in the sector of non-residential buildings in Latvia are comparatively rare, as the attention is mostly focused on residential buildings. However, it has to be noted that non-residential buildings form a considerable part of the building stock and the increase of their energy performance can bring a significant contribution in achieving the national targets.

## 2. CURRENT SITUATION AND PROBLEMS

Structure usage types are prescribed by Cabinet Regulation No 326 "Structure Classification Regulations" [8]. All structures are divided into two parts – buildings and engineering structures. Buildings are divided into residential and non-residential.

The main groups of non-residential buildings, in accordance with Regulation No 326, are as follows:

- Hotels and similar usage buildings (code 121);
- Office buildings (code 122);
- Wholesale and retail trade buildings (code 123);
- Transport and communication buildings (code 124);

- Industrial buildings and warehouses (code 125);
- Public entertainment, education, hospital or institutional care buildings (code 126);
- Other non-residential buildings (code 127).

In accordance with the State Land Service data [9], 1373642 buildings were registered in Latvia as of 1 January 2022, of which 368038 (26.8 %) were residential and 1005604 (73.2 %) non-residential. All buildings occupy the area of 206.6 million $m^2$; residential buildings occupy 91.1 million $m^2$ (44.1 %) and non-residential 115.5 million $m^2$ (55.9%). Division of non-residential buildings by groups according to their number and area is provided in Fig. 1.

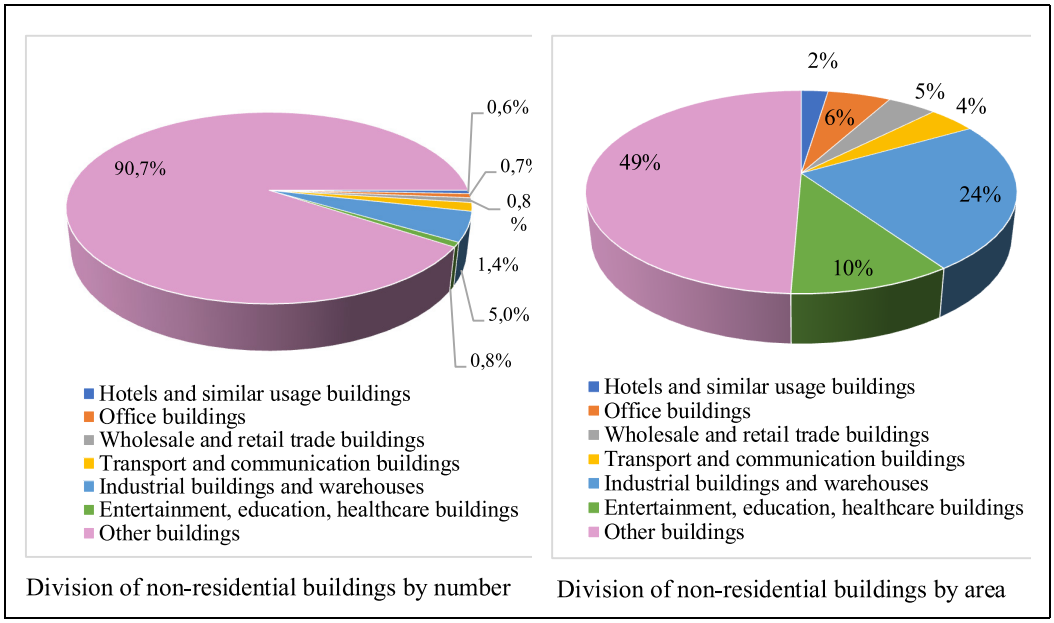


*Fig. 1.* Proportion of non-residential buildings by number and area [9].

The bulk of non-residential buildings – 913.1 thousand or 90.7 % – are other non-residential buildings, which are buildings of penal institutions, prisons, defence forces, border guards, police and fire fighting services, water closets, outbuildings of households, individual garages, individual baths, cellars, summer kitchens, greenhouses, security guards, gatehouses, individual garden houses, outhouses not otherwise classified, etc. The next biggest group is represented by industrial buildings and warehouses (50.4 thousand or 5.0 %) and transport and communication buildings (14.5 thousand or 1.4 %). The number of buildings in other groups (hotels, offices, educational, healthcare, wholesale and retail trade and sport buildings) fluctuates from 5 to 8 thousand.

When analysing the division by area, other non-residential buildings form about a half (57.0 million $m^2$ or 49.4 %), industrial buildings and warehouses – about 27.3 million $m^2$ or 23.6 %, entertainment, education and healthcare buildings together – about 11.9 million $m^2$ or 10.3 %. Other groups of buildings occupy the area of 2–6 million $m^2$.

**Table 1.** New and Reconstructed Non-residential Buildings (2010–2021), thsd. m$^2$ [10]

| Groups of buildings | Total non-residential buildings | New | | Reconstructed | |
|---|---|---|---|---|---|
| Hotels and similar usage buildings | 2770 | 255.0 | 9.2 % | 245.0 | 8.8 % |
| Office buildings | 6530 | 260.5 | 4.0 % | 601.6 | 9.2 % |
| Wholesale and retail trade buildings | 5080 | 526.8 | 10.4 % | 809.0 | 15.9 % |
| Transport and communication buildings | 4950 | 200.6 | 4.1 % | 88.1 | 1.8 % |
| Industrial buildings and warehouses | 27280 | 2380.4 | 8.7 % | 2001.8 | 7.3 % |
| Entertainment, education and healthcare buildings | 11870 | 488.3 | 4.1 % | 2727.7 | 23.0 % |
| Other buildings | 57010 | 1908.7 | 3.3 % | 972.6 | 1.7 % |
| **Total** | **115490.0** | **2380.4** | **2.1 %** | **11085.7** | **9.6 %** |

When looking at statistical data [10] about new and reconstructed non-residential buildings during the period from 2010 to 2021 (Table 1), only 2.1 % new buildings were built and 9.6 % were reconstructed from the total area of non-residential buildings. Public entertainment, educational, healthcare and wholesale and retail trade buildings prevail among new and reconstructed ones.

During the period from 2008 to 2020, commercial and public sectors, which include hotels and restaurants, offices, wholesale and retail trade, educational, healthcare and sport buildings, on average consumed about 24.8 PJ of energy a year and households – 53.3 PJ.

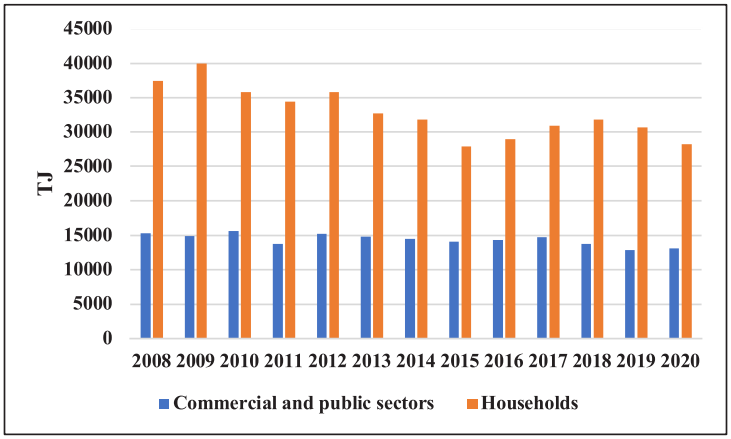


*Fig. 2.* Final energy consumption for space heating, TJ [12].

When taking into account final consumption of electric energy (electric energy consumption for ensuring heating is not taken into account), which is mostly used for lighting and operation of different devices, then commercial and public sectors on average consumed 15.1 PJ of energy a year and households – 46.9 PJ. It can be counted that this energy was consumed for heating of premises and preparing hot water. The consumption of commercial and public sectors forms about 44 % of that of households.

The calculations took into account that a certain amount of energy was consumed for preparing hot water, which did not influ-

ence the building heating indicators. It was assumed that on average 25–30 % of energy resources were consumed for preparing hot water at households [11] and on average 5 % – in commercial and public sectors. The final energy consumption of commercial and public sectors in comparison with households is provided in Fig. 2.

In the context of energy performance of buildings, attention should be paid to non-residential buildings which are heated. The Long-term Strategy for Building Renovation mentions that out of all non-residential buildings only about 7.5 % or 75 thousand are provided with heating [5]. The area of these buildings is about 27 million $m^2$.

Groups of non-residential buildings, which are heated:

- Hotels and restaurants;
- Office buildings;
- Wholesale and retail trade buildings;
- Buildings of educational institutions;
- Buildings of healthcare institutions;
- Sport buildings;
- Other type of buildings where energy is consumed.

The number and area of the aforementioned groups of buildings are provided in Table 2.

**Table 2.** Number and Area of Non-Residential Buildings in the Group of Heated Buildings [9], [5]

| **Groups of buildings** | **Number** | | **Area, mln.$m^2$** | |
|---|---|---|---|---|
| Hotels and restaurants | 2928 | 11.2 % | 2.35 | 9.1 % |
| Office buildings | 7124 | 27.3 % | 6.53 | 25.3 % |
| Wholesale and retail trade buildings | 8089 | 31.0 % | 5.08 | 19.7 % |
| Educational buildings | 3791 | 14.5 % | 6.93 | 26.8 % |
| Healthcare buildings | 1340 | 5.1 % | 2.02 | 7.8 % |
| Sport buildings | 1048 | 4.0 % | 1.24 | 4.8 % |
| Other buildings | 50700 | 67.6 % | 2.95 | 10.9 % |
| | **75020** | **100.0 %** | **27.10** | **100.0 %** |

Other type of non-residential buildings presents the biggest number of heated non-residential buildings; however, their area in general is not large – only about 11 %. The biggest proportion according to the area is for educational, office and wholesale and retail trade buildings.

As of 1 January 2020, the Latvian Construction Standard LBN 002-19 "Thermotechnics of uilding Envelopes", approved by the Cabinet Regulation No 280 adopted on 25 June 2019, took effect. From 1 January 2021, all new buildings must comply with the requirements of the almost zero-energy building (Table 3).

**Table 3.** Minimum Allowed Energy Efficiency Level for New Buildings, Renovation and Reconstruction of Buildings [13]

| Documentation acceptance period of a building construction project | For residential buildings | | For non-residential buildings | |
|---|---|---|---|---|
| | Multi-dwelling houses | One- or two-dwelling houses | Buildings owned by the state or local governments | Other non-residential buildings |
| **Minimum allowed energy efficiency level for new buildings** | | | | |
| From 1 January 2021 | almost zero-energy building | almost zero-energy building | almost zero-energy building | almost zero-energy building |
| **Minimum allowed energy efficiency level for renovation and reconstruction of buildings, kWh/$m^2$ a year** | | | | |
| From 1 January 2021 | ≤ 80 | ≤ 90 | ≤ 90 | ≤ 100 |

The requirements for the almost zero energy building are set by Cabinet Regulation No 222 "Building Energy Performance Calculation Methods and Building Energy Certification Regulations" [14]. With regards to energy consumption for heating, the consumption of such building may not exceed the level for the A class building. Also, the consumption of the primary non-renewable energy of the building may not exceed the values for the A class building. Devices consuming energy of engineering systems installed in the building must comply with the eco-design requirements and their energy marking – of at least A class. Moreover, compliance of the microclimate of premises with the construction regulatory enactments and requirements in the field of hygiene and occupational safety must be ensured in the building (Table 4).

**Table 4.** Minimum Allowed Heating Consumption Level of the Building Energy Performance, kWh/m$^2$ a Year [14]

| Building energy performance class | Residential and non-residential buildings | | Residential buildings | Non-residential buildings | |
|---|---|---|---|---|---|
| | Heated area, m$^2$ | | | | |
| | 50–120 | 120–250 | Over 250 | | |
| | | | Residential houses | Offices, educational institutions, hotels, restaurants, sport and commercial buildings | Hospitals |
| A | ≤60 | ≤50 | ≤40 | ≤45 | ≤50 |
| B | ≤75 | ≤65 | ≤60 | ≤65 | ≤70 |
| C | ≤95 | ≤90 | ≤80 | ≤90 | ≤100 |
| D | ≤150 | ≤130 | ≤100 | ≤110 | ≤120 |
| E | ≤180 | ≤150 | ≤125 | ≤150 | ≤160 |
| F | >180 | >150 | >125 | >150 | >160 |

Until 2021, to determine the energy performance class, buildings were divided into 'residential' and 'non-residential' and all residential houses of A class were set the requirement not to exceed 40 kWh/m$^2$ a year and all non-residential buildings – 45 kWh/m$^2$ a year. Starting from 2021, the heated area of the building has been also taken into account. For buildings with the area of 50–120 m$^2$, the minimum allowed heating consumption level for the A class building is 60 kWh/m$^2$, for buildings with the area of 120–250 m$^2$, it may not exceed 50 kWh/m$^2$ and for larger buildings – 40 kWh/m$^2$. For non-residential buildings, except for hospitals, the heating consumption level for the A class building may not exceed 45 kWh/m$^2$ and for hospitals – 50 kWh/m$^2$ a year.

## 3. DISCUSSION AND RESULTS

Energy certification of buildings in Latvia was started in 2010. Cabinet Regulation No 504 (8 June 2010) "Regulations on Energy Certification of Buildings" was issued that year. In 2013, the Regulation was replaced by Regulation No 383 (9 July 2013) "Regulations on Energy Certification of Buildings", and Cabinet Regulation No 222 (8 April 2021) "Building Energy Efficiency Calculation Methods and Building Energy Certification Regulations" took effect in 2021.

Until 2016, energy certificates were issued in paper form, and there are no data

available regarding how many and what type certificates were issued during that period. Since 2016, independent experts have been registering energy performance certificates of buildings in the Building Information System (BIS) [15]. Thus, these energy performance certificates and basic data included there are publicly accessible. As of 1 August 2022, BIS had 332 such historical energy performance certificates of buildings registered, of which 281 are in force. However, the content of these certificates is not available and they cannot be used in the research.

In accordance with the Law on the Energy Performance of Buildings [16], energy certification is performed for the following buildings:

- for a building to be designed, rebuilt, or renewed in order to accept it for service or sell it;
- for an existing building in order to sell, rent, or lease it;
- in cases where a building owner has taken a decision on certification of the energy performance of the building;
- for a public building the area of inside premises of which exceeds 250 $m^2$ and which is used by a state or local government institution.

The research uses the list of building energy performance certificates of the State Construction Control Bureau of Latvia published on the Latvian Open Data Portal [17] and the Building Information System [15].

The statistics of building energy performance certificates, in general, for the period of 2016–2020 was researched in the project "Analysis of Actual Energy Consumption of Almost Zero Energy Buildings and Development of the Required Energy Efficiency Increase Solutions" No 1.1.1.2/VIAA/3/19/505. It was noted in the publication [18] that documents with the expired validity were erroneously included in the list of valid temporary energy performance certificates. It also has to be noted that there is a lot of erroneous information regarding 2021: (1) when searching for energy performance certificates in BIS, a list appears with a big number of temporary energy performance certificates; (2) in the Open Data Portal, data on 2021 are entered incompletely.

As of the start of 2022, 4241 energy performance certificates were registered in the BIS energy performance certificate register (this number does not include building temporary energy performance certificates), of which 1789 (42.2 %) are for residential buildings and 2452 (57.8 %) for non-residential buildings (Fig. 3).

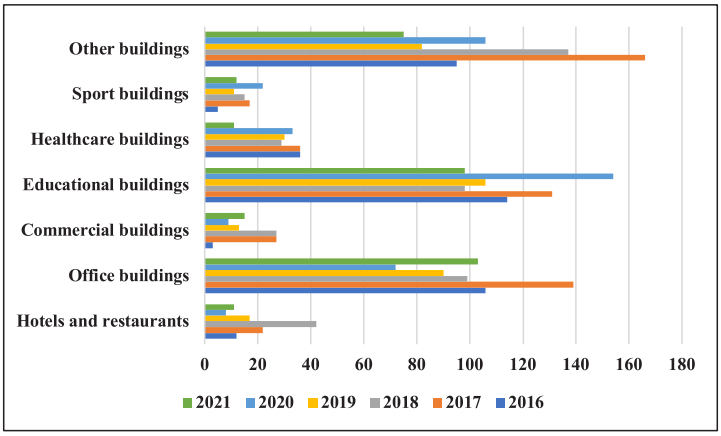


*Fig. 3.* Division of energy performance certificates of non-residential buildings by year and type of buildings.

Energy performance of non-residential buildings has been evaluated based on the data of energy performance certificates. The total amount of the considered data forms a comparatively small part (see Fig. 4) of the total number of buildings; however, it is sufficiently large to characterise the situation with non-residential buildings in general and to make general conclusions.

Figure 4 demonstrates the proportion of energy performance certificates registered in BIS in each group of non-residential buildings. The biggest number of energy-certified buildings is between educational institutions (18.8 %) and healthcare institutions (13.3 %), as well as office buildings (8.7 %) and sport buildings (7.7 %).

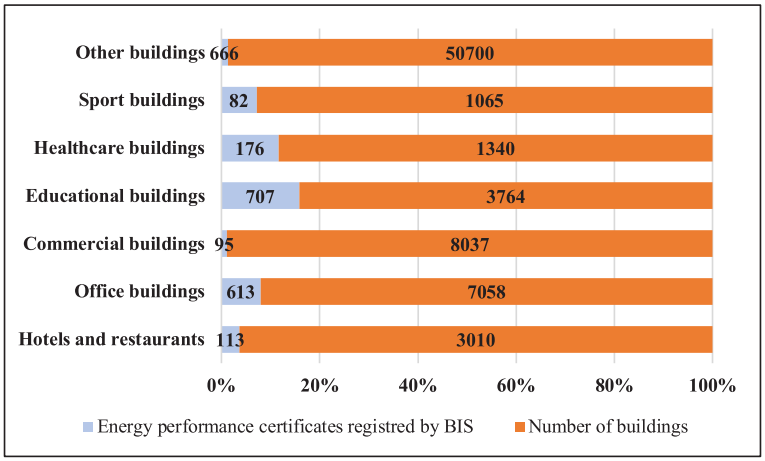


*Fig. 4.* Proportion of energy-certified buildings.

Figure 5 demonstrates the number of energy performance certificates registered in BIS in each group of non-residential buildings. In the sector of non-residential buildings, the biggest number of energy performance certificates during the period of 2016–2022 is registered for educational institutions (28.8 %) and office buildings (25.0 %). The largest proportion is formed by the group of other buildings (27.2 %), which are not included in any of the aforementioned categories.

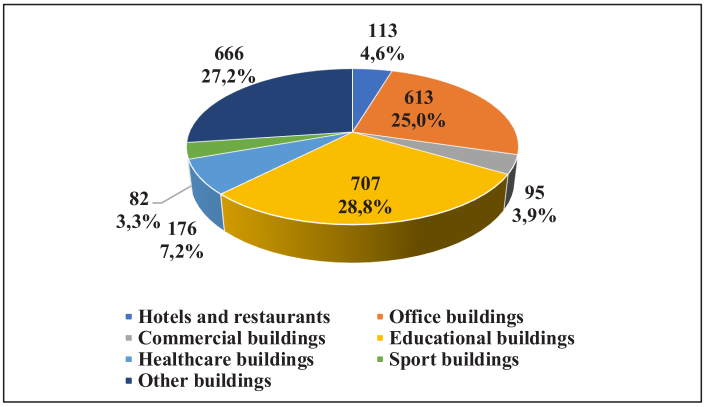


*Fig. 5.* Division of the number of building energy performance certificates by the type of non-residential buildings.

In accordance with the Structure Classification Regulations, office buildings are the ones used for transactions and different administrative purposes, including banks, post offices, publishing houses, local government institutions, state administration institutions, buildings of companies, institutions and other organisations, as well as conference and congress centres, court and parliament buildings. The biggest number of energy performance certificates for office buildings can be explained by the fact that this group includes state and local-government buildings for which energy certification is compulsory. Similarly, a big part of educational and healthcare institution buildings belongs to the state or local governments.

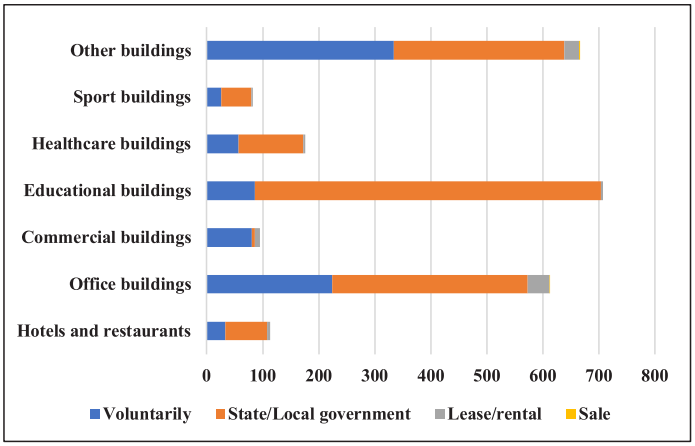


*Fig. 6.* Purpose of building energy performance certification.

Figure 6 confirms the aforementioned fact on compulsory energy performance certification of state or local government buildings. Besides, the fact should also be mentioned that an energy performance certificate is a compulsory requirement to submit an application for receiving co-financing from the EU funds.

For the biggest part (61.9 %) of non-residential buildings, the purpose of energy performance certification is that the building belongs to the state or a local government or a state or local government institution is located there. The purpose of issuing 34.3 % of energy performance certificates is voluntary energy performance certification and only in 3.7 % of cases an energy performance certificate was required to sell or lease a building. Voluntary energy performance certification also includes cases when co-financing from the EU funds is planned to be attracted for a building.

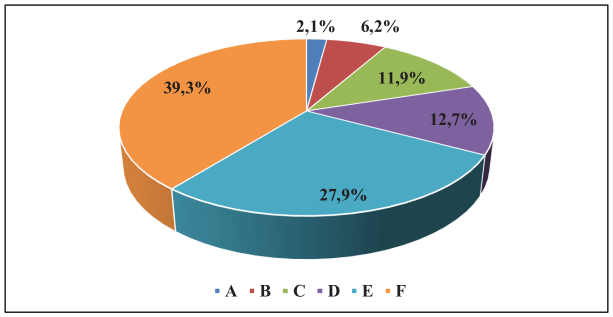


*Fig. 7.* Division of energy performance classes of non-residential buildings.

Figure 7 demonstrates a summary on energy performance classes of non-residential buildings. The biggest proportion (39.3 %) is for buildings of the lowest F class. A similarly big number (27.9 %) of buildings have the E class. 11.9 % and 12.7 % of non-residential buildings have respectively C and D classes. Whereas 6.2 % of buildings correspond to the B class, and only 2.1 % of buildings – to the A class.

Figure 8 summarises information on energy performance heating consumption classes of non-residential buildings by the group of buildings.

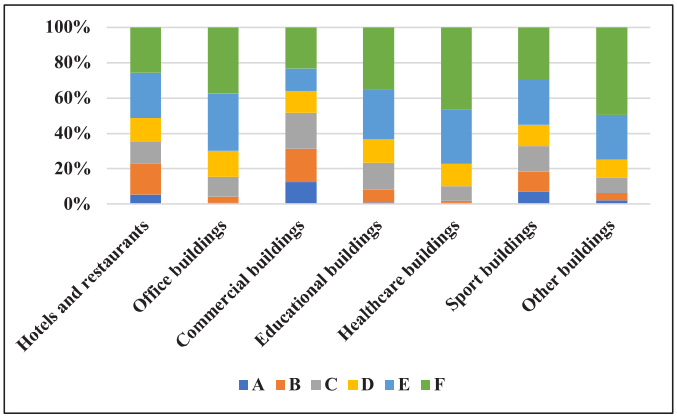


*Fig. 8.* Energy performance levels of non-residential buildings by the group of buildings.

When analysing the energy performance classes by the group of buildings, one can conclude that the highest energy performance class is at wholesale and retail trade buildings, as well as hotels and restaurants. They are followed by sport and educational buildings, and the lowest class is at office, healthcare and other buildings. As there is no information available regarding what are these other buildings, it is not possible to analyse this group of buildings more comprehensively.

**Table 5.** Average Energy Performance Levels and Classes of Non-residential Buildings

| Group of buildings | Energy consumption for heating, kWh/m$^2$ | Energy performance class |
|---|---|---|
| Hotels and restaurants | 116 | E |
| Office buildings | 142 | E |
| Wholesale and retail trade buildings | 104 | C |
| Educational buildings | 137 | E |
| Healthcare buildings | 158 | E |
| Sport buildings | 128 | E |
| Other buildings | 173 | F |
| Non-residential buildings | 137 | E |

In all groups of non-residential buildings, except for wholesale and retail trade buildings and other buildings, the energy performance class is E. At wholesale and retail trade buildings, it corresponds to the C class and at other buildings to the F class. The average energy performance class of non-residential buildings is E (Table 5).

## CONCLUSIONS

One of the trends for reducing energy consumption is to increase energy performance of buildings. In compliance with the EU and Latvian political statements, it is required to promote renovation of residential and non-residential buildings.

Studies regarding energy performance aspects in the sector of non-residential buildings in Latvia are comparatively rare; however, final consumption of energy at heated non-residential buildings forms about 44 % of that of residential buildings. Therefore, the increase of their energy performance can bring a significant contribution in achieving the national targets.

Having researched 2452 energy performance certificates of non-residential buildings for the period of 2016–2021, one can conclude that the biggest number of energy-certified buildings of the total number of non-residential buildings is between educational institutions (18.8 %) and healthcare institutions (13.3 %), as well as office buildings (8.7 %) and sport buildings (7.7 %).

In the sector of non-residential buildings, the biggest number of energy performance certificates during the period of 2016–2022 was registered for educational institutions (707 or 28.8 %) and office buildings (613 or 25.0 %).

The purpose of energy performance certification for the biggest part (61.9 %) of non-residential buildings is that the building belongs to the state or local government, or a state or local government institution is located there (energy performance certification for such buildings is compulsory). The purpose of issuing 34.3 % of energy performance certificates is voluntary energy performance certification (voluntary energy performance certification also includes cases, when co-financing from the EU funds is planned to be attracted for a building renovation) and only in 3.7 % of cases an energy performance certificate was required to sell or lease the building.

With regards to energy performance classes, the biggest proportion (39.3 %) is for buildings of the lowest F class. A similarly large number (27.9 %) of buildings have the E class. 11.9 % and 12.7 % of non-residential buildings have respectively C and D classes. 6. 2% of buildings correspond to the B class, and only 2.1 % of buildings – to the A class.

The highest energy performance class is at wholesale and retail trade buildings, as well as hotels and restaurants. They are followed by sport and educational buildings, and the lowest class is at office, healthcare and other buildings.

In all groups of non-residential buildings, except for wholesale and retail trade and other buildings, the energy performance class is E. At wholesale and retail trade buildings, it corresponds to the C class and at other buildings to the F class. The average energy performance class of non-residential buildings is E.

Up to now, co-financing from the EU funds and other financial support instruments to increase energy performance of non-residential buildings has been mostly provided to the public sector – state and local government buildings. In the future, it would be required to anticipate support also for the commercial sector buildings regardless of their trend of business activity and the industry (hotels, restaurants, offices, as well as educational, healthcare and sport buildings, etc., which are not state and local government buildings), with account of the fact that they form a big part of the segment of non-residential buildings [5].

## REFERENCES


1. Ministry of Environmental Protection and Regional Development of the Republic of Latvia (2020). *Informative Report "Strategy of Latvia for the Achievement of Climate Neutrality by 2050*". Available at https://unfccc.int/sites/default/files/resource/LTS1_Latvia.pdf
2. Eur-Lex (2020). Directive 2010/31/EU of the European Parliament and of the Council of 19 May 2010 on the energy performance of buildings. Available at https://eur-lex.europa.eu/legal-content/EN/TXT/?uri=celex:32010L0031
3. Eur-Lex (2018). *Directive (EU) 2018/844 of the European Parliament and of the Council of 30 May 2018 amending Directive 2010/31/EU on the energy performance of buildings and Directive 2012/27/EU on energy efficiency*. Available at https://eur-lex.europa.eu/legal-content/EN/TXT/?uri=uriserv%3AOJ.L_.2018.156.01.0075.01.ENG
4. Eur-Lex (2018). *Regulation (EU) 2018/1999 of the European Parliament and of the Council of 11 December 2018 on the Governance of the Energy Union and Climate Action (2018)*. Available at https://eur-lex.europa.eu/eli/reg/2018/1999/oj/?locale=en
5. Ministry of Economy (2020). *Informative Report "Long-term Strategy for Building Renovation"*. Available at https://energy.ec.europa.eu/system/files/2021-01/lv_2020_ltrs_official_translation_en_0.pdf
6. Ministry of Economy (2020). *National Energy and Climate Plan for 2021-2030.* Available at https://ec.europa.eu/energy/sites/ener/files/documents/lv_final_necp_main_en.pdf
7. Krmiņš, Ē., Dimdina, I., & Lešinskis, A. Heat energy consumption in not renovated buildings and in buildings after partial renovation. In: *Civil Engineering '11: 3rd International Scientific Conference: Proceedings* (pp. 227–235), 12–13 May, 2011. Jelgava: Latvia University of Agriculture, Latvia. ISSN 2255-7776.
8. Cabinet Regulation No 326 (2018). *Structure Classification Regulations.* Available at https://likumi.lv/ta/id/299645-buvju-klasifikacijas-noteikumi
9. Valsts zemes dienests (2021). *Reģistrēto būvju skaits sadalījumā pa galvenajiem lietošanas veidiem.* Available at https://www.vzd.gov.lv/lv/registreto-buvju-skaits-sadalijuma-pa-galvenajiem-lietosanas-veidiem
10. Official Statistical Portal (2022). *Commissioned Buildings by Building Type, Region and City.* Available at https://data.stat.gov.lv/pxweb/en/OSP_PUB/START/BUE030
11. RTU Institute of Environmental Protection and Heat Systems (2018). *Latvijas siltumapgādes un aukstumapgādes efektivitātes potenciāla noteikšana atbilstoši direktīvai 2012/27ES par energoefektivitāti.* Available at https://energy.ec.europa.eu/system/files/2021-10/lv_ca_2020_lv.pdf
12. Official Statistical Portal (2022). *Energy Balance.* Available at https://data.stat.gov.lv/pxweb/en/OSP_PUB/START__NOZ__EN__ENB/ENB060
13. Cabinet Regulation No. 280 (2019). *Regulations Regarding the Latvian Construction Standard LBN 002-19, Thermotechnics of Building Envelopes.* Available at https://likumi.lv/ta/en/en/id/307966-regulations-regarding-the-latvian-construction-standard-lbn-002-19-thermotechnics-of-building-envelopes
14. Cabinet Regulation No. 222 (2021). *Ēku energoefektivitātes aprēķina metodes un ēku energosertifikācijas noteikumi.* Available at https://likumi.lv/ta/id/322436-eku-energoefektivitates-aprekina-metodes-un-eku-energosertifikacijas-noteikumi
15. Building Information System (2022). *Ēku energosertifikātu reģistrs.* Available a: https://bis.gov.lv/bisp/lv/epc_documents
16. Legal Acts of the Republic of Latvia (2012). *Law on the Energy Performance of Buildings.* Available at https://likumi.lv/ta/en/en/id/253635-law-on-the-energy-performance-of-buildings

17. Latvian Open Data Format (2022). *Ēku energosertifikātu saraksts*. Available at https://data.gov.lv/dati/eng/dataset/bis_swkx3qxubp9g-wp_zpvciq

18. Gendelis, S. (2021). Ēku energosertifikāta statistika. *Būvinženieris*, *78*, 133–138. Available at https://modinst.lu.lv/wp-content/uploads/2021/03/Energosertifikati_BI78.pdf

sciendo

LATVIAN JOURNAL OF PHYSICS
AND TECHNICAL SCIENCES
2022, N 6

DOI: 10.2478/lpts-2022-0046

# DETERMINING THE EFFECT OF LOAD ON SYNCHRONOUS GENERATOR WITH SPARK-IGNITION ENGINE ENERGY EFFICIENCY

S. Zaichenko[1*], A. Dychko[1], U. Ercetin[2], V. Opryshko[1], A. Kleshchov[1]

[1] Institute of Energy Saving and Energy Management,
National Technical University of Ukraine
"Igor Sikorsky Kyiv Polytechnic Institute"
37 Peremohy Ave., Kyiv, 03056, UKRAINE
[2] Dumlupinar University
Merkez Kampüsü Tavsanlı Yolu10 km, Kutahya, 43040, TURKEY
*email: zstefv@gmail.com

The paper presents a new approach to energy indicator determination, such as specific fuel consumption and energy efficiency of the power plant. The essence of the new method is to determine the instantaneous power of the installation with subsequent data processing. The use of this method allows establishing the dependence of specific energy indicators on the generating unit load levels. The established distribution allows defining optimum parameters of experimental setup and consumption at various loading levels. The highest specific energy consumption of fuel is observed (1189–1297 g / (kW·h) and 962–1147 g / / kW·h)) at the lowest and the highest load for different fuels. Experimental data show that fuel without ethanol impurities can generate more electricity, which should be used at higher demand.

***Keywords:*** *Braking specific fuel consumption, energy efficiency, power plants, spark ignition engine.*

## 1. INTRODUCTION

World's energy strategy supports the course of rational "minimization" of energy, in particular, in Ukraine a significant increase in the share of renewable energy sources and off-balance energy resources to 57.73 million toe at the level of 2030 compared to 15.51 million toe used in 2005 (an increase of 3.72 times). It was forecast that electricity production by power plants using renewable energy sources for Ukraine (excluding elec-

tricity production at small hydropower plants and biofuels in the baseline scenario) would grow to 50 million kWh in 2010; 800 – in 2015; 1500 – in 2020; 2000 million kWh – in 2030. At the same time, electricity production by industrial and municipal power units will increase to 9.85 billion kWh in 2010; 10.8 – in 2015; 11.4 – in 2020; 13.5 billion kWh in 2030 [1], [2]. Analysis of the dynamics and structure of Ukraine's electricity production over the past two years (2019–2020) shows a steady increase in the share of autonomous power generation in total electricity production from 1 to 2 %, respectively 2372 million kWh and 5 357 million kWh.

This feature is explained by the development of autonomous power supply systems, which not only complement stationary power plants, but in many cases provide solutions to important technical problems of power supply in hard-to-reach areas. Autonomous energy allows consumer not to depend on the centralized energy supply and to use the technology, optimal for these conditions as SmartGrid source of energy production [3]. In different modes of the power supply system, electric generators usually operate with a load less than the nominal. This is due to the need for a reserve to provide electricity to different numbers of energy consumers.

Analysis of autonomous energy sources market, which becomes the most widespread, shows a fairly narrow range of used generators [4]. The most common variant of an autonomous energy source (more than 50 % of all units) is gasoline generators with spark ignition with a synchronous electric generator of 2.5–3.5 kW.

The actual efficiency of the generator unit in case of underload depends on the efficiency of the engine and the efficiency of the synchronous generator at different loads. There are a number of methods for setting these parameters for both internal combustion engines (ISO 15550: 2016) and for synchronous generators (DSTU IEC 60034-2-1: 2019). However, the application of these methods for autonomous generators is complicated by individual components, the internal combustion engine and the generator, which in some cases are impossible to define due to its design. That is why the consideration of the system states, as a whole, needed to facilitate the process of setting the parameters of engine-generator system.

To use this approach, it is necessary to modernize existing research methods of autonomous electrical installations at different load levels, which are generally aimed at determining the quality of power supply in nominal operating modes or close to nominal (overload).

## 2. REVIEW OF SCIENTIFIC SOURCES

A number of works, which can be divided into two main groups, are devoted to the analysis of energy efficiency parameters of installations based on internal combustion engines. The first group considers the process of determining the energy parameters by studying mainly the characteristics of the internal combustion engine. In this case, as a characteristic of energy efficiency using the ratio of fuel consumption rate to engine power is brake-specific fuel consumption. This approach is based on the fact that the main losses of installations fall on the internal combustion engine [5]. The second group of studies is devoted to power plant as a whole, in some cases considering the energy performance of system components. Energy efficiency in this case is assessed by the ratio of generated power and fuel consumption. A character-

istic common feature for these studies is the determination of energy efficiency indicators of installations with load variation. Also for both research groups for internal combustion engine load is connected to the electromechanical loader – an electric brake or the generator.

Among total scope of research of the first group in terms of detailing the description, setting tasks and conducting research, it is possible to note the works devoted to use of alternative fuels with mineral fuel mixtures. These studies mainly experimentally investigate the influence of various factors (the ratio of biofuels and mineral fuels, gas and liquid fuels, speed, angle of advance of the spray or ignition) on energy performance. The main goal of these studies is to confirm the possible reliable and safe use of alternative fuels for the environment. A number of studies note the independence of costs on the power plant level [6].

In [7], the authors aimed at operation optimization of the power plant using a mixture of fuels (hydrogen and gasoline) as the main factors for the concentration of fuels and the speed of the generator internal combustion engine shaft. A characteristic of the established pattern is the optimal efficiency value change at different concentrations of the mixture and the load, which allows optimising the generation process by using different mixtures. To determine the conditions that correspond to the optimal value, most experiments were conducted at the minimum installation power values of 2.5 kW (<50 %) and did not cover the entire possible range.

In [8], the authors aimed at studying the efficiency of a spark ignition engine by converting the thermal energy of exhaust gases into electricity using a thermoelectric generator, thus investigating the issue of the power plant energy efficiency increase [8]. When power increases from 25 to 75 kW, there is no significant change in specific fuel consumption (within 3 %), which differs significantly from the known data.

The general characteristics of the presented studies include the rarity of the described fuel mixtures and methods of electricity generation usage. Little attention is paid to the conditions of the experiment, the influence of engine parameters, rheological parameters of the fuel, namely the density of the fuel. Also, the studied models of autonomous generators and motors have a narrow use for power supply as backup sources.

Given above, it is possible to conclude that it is necessary to study the energy performance of a common generator type, namely a synchronous generator with a spark ignition engine. Also, special attention should be paid to the type and conditions of fuel use, which are maximally represented at the market.

The aim of the study is to determine the energy performance of autonomous electric generators based on spark ignition engines using the most common fuels.

## 3. DESCRIPTION OF RESEARCH METHODS

Energy indicators that are necessary for modeling power supply system dynamics and technical and economic assessment of setup options for new power systems belong to:

- fuel consumption for electricity generation at different load levels, g / kWh;
- efficiency at different load levels.

Two types of the most common used fuels for the conducted experiments:

- gasoline automobile A-95 - Euro5;
- gasoline automobile A-95 - Euro5 - E7.

The experiments were performed indoors at a temperature of (298 ± 3) K [(25 ± 3) ° C] and relative humidity (95 ± 3) %. The value of atmospheric pressure was in the range of 755–165 mm Hg. Art. (100 658–101 991 Pa). Under these conditions, one of the main rheological parameters of the fuel, density, was determined. Thus, for A-95 - Euro5 it was 735 kg / m3, and for A-95 - Euro5 - E7 – 757 kg / m3.

Among the wide range of autonomous generators, the authors paid attention to generating units based on a single-cylinder gasoline four-stroke internal combustion engine with an engine displacement of 200 $cm^3$. Technical characteristics are given in Table 1. Most generators use as an alternator a synchronous generator with automatic voltage regulator (AVR), which contains the rotor and stator windings. The rotor speed of the generator is maintained by a centrifugal frequency regulator connected to the carburetor.

The research notes the growth of a part of production by powerful autonomous stations and by small stations of public utilities. The chosen generator has the most common design among existing generators, as it is pointed, due to its simplicity of design and cost. The generator design is a copy of the Honda generator. Considered above, the collection of data is important for determining the quality indicators of power supply for various objects.

**Table 1.** Technical Characteristics of the Synchronous Electric Generator with the Spark Ignition Engine

| **Parameter** | **Unit** | **Value** |
|---|---|---|
| Engine type | - | 4-stroke gasoline engine with air cooling OHV |
| Number of cylinders | pcs | 1 |
| Engine model | - | H-168 |
| Engine displacement | $cm^3$ | 196 |
| Internal combustion engine power | W | 4780 |
| Maximum power of the electric generator | W | 2800 |
| Fuel tank volume | $m^3$ | 0.015 |
| Oil sump volume | $m^3$ | 0.0006 |
| Generator weight | kg | 53.6 |

Figure 1 demonstrates a schematic representation of the experimental setup, as well as measuring devices on it. The basis of the experimental setup is an autonomous electric synchronous generator – 1 with a spark ignition engine – 2. The carburetor of the engine – 3 is disconnected from the tank (not shown) and connected to the vessel with the divisions marked on it – 4. Synchronous generator – 1 is connected to the loader in the form of a liquid rheostat – 5. Power measurement is performed by registering the voltage on the generator panel and Hall's current sensor – 6. Analog signal from the current sensor YHDC HK 16 and voltage sensor based on inductive module with voltage transformer series ZMPT101B is converted by 14-bit data acquisition microsystem DAQ12 – 7 with fixing on the computer – 8.

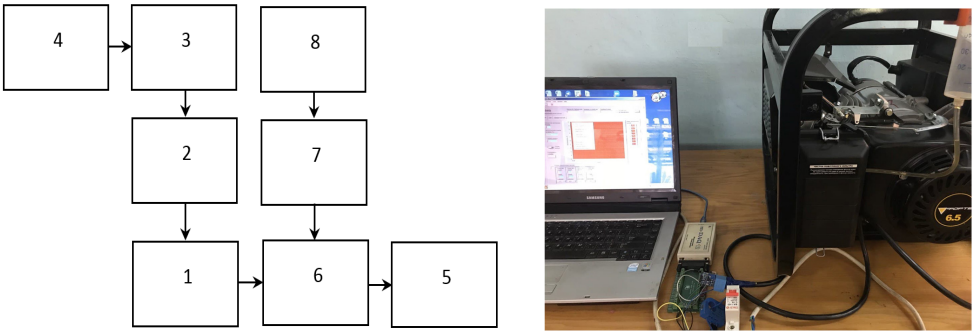


*a* *b*

*Fig. 1.* Scheme of the experimental setup for determining the energy parameters of a synchronous electric generator with a spark ignition engine.

The process of electricity generation by a synchronous generator with a direct kinematic connection to the motor depends on a number of factors that significantly affect the quality. Among the main factors that significantly affect the voltage and current should be noted the type of load and stability of the engine crankshaft. In our case, the active load is used as a load, which minimizes the possible voltage phase shift. At the same time, it is possible to note at loading of the generator essential curvature of a sinusoid with emergence of harmonics of various order with asymmetry and deviation of frequency from the nominal value (to 7 %) (Fig. 2). Increasing the load from 500 W to 1500 W leads to 30 % sinusoidal distortion.

To determine the energy consumption, the RMS voltage can be used, which is the result of periodic function integration:

$$\Delta P = \frac{\int_0^T (U(t))^2\, dt}{R} = \frac{\int_0^T \left(U_m \sin(2\pi \frac{t}{T})\right)^2 dt}{R} = \frac{TU_m^2}{2R} = \frac{TU_{rms}^2}{R}, \quad (1)$$

where

$T$ is the period of voltage fluctuations; $U(t)$ is the voltage change function.

Due to these distortions, the real diagram with increasing load in a certain approximation for some areas can be described as straight. In this case, energy consumption for the period is as follows:

$$\Delta P = \frac{\int_0^T (U(t))^2\, dt}{R} = 4\frac{\int_0^T \left(\frac{U_m}{T/4} t\right)^2 dt}{R} = \frac{TU_m^2}{3R}. \quad (2)$$

Comparison of the obtained values shows that the calculation error can be 30 % of the generator nominal power.

From the above, it is obvious that determining the amount of electrical energy, the use of the ratios of maximum values and root mean square values of voltage and current leads to significant errors in the calculation. More accurate values in determining the amount of electrical energy can be achieved by taking into account the instantaneous change in power.

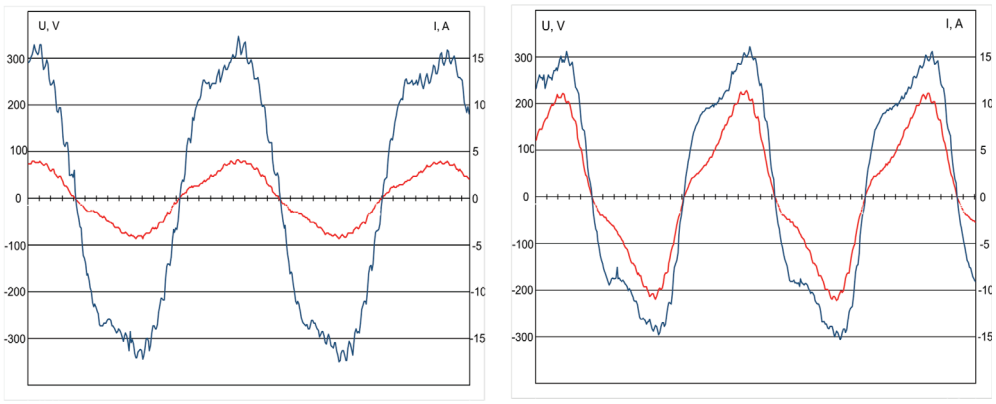


*a* *b*

*Fig. 2.* Voltage change diagrams (———) and current (———) at different load for (gasoline automobile A-95 - Euro5):
a – generator load 500W;
b – generator load 1500W.

In the general case, the energy balance of the diagnostic system is as follows:

$$\Delta Q - (\Delta A + \Delta P) = 0, \tag{3}$$

where

$Q$ – fuel combustion energy;
$\Delta P$ – useful work in the form of electricity;
$\Delta A$ – total thermal, mechanical and electrical energy losses.

Combustion energy is determined by volumetric measurement of fuel for a certain time of generator operation $\Delta t$:

$$\Delta Q = q \rho \Delta V, \tag{4}$$

where
q – specific heat of combustion;
ρ – fuel density;
$\Delta V$ – amount of fuel consumed by the generator during operation $\Delta t$.

During the operation of the generator based on the internal combustion engine, the voltage and current values change significantly over time due to fluctuations in the speed of the crankshaft, which needs to be clarified when determining the power while operation. Useful work in the form of electricity depends on the level of current and voltage:

$$\Delta P = \int_0^{\Delta t} P'(t)dt = \int_0^{\Delta t} I(t)U(t)dt\,. \tag{5}$$

Specific fuel consumption for electricity generation:

$$BSFC = \frac{m}{\Delta P} = \frac{\rho \Delta V}{\Delta P} = \frac{\rho \Delta V}{\int_0^{\Delta t} I(t)U(t)dt}\,. \tag{6}$$

The presented dependence of the definition allows determining with high accuracy the energy performance of a synchronous generator with a spark ignition engine by taking into account fluctuations in current and voltage levels.

Efficiency at different load levels:

$$\eta = \frac{\Delta P}{\Delta Q} = \frac{\int_0^{\Delta t} I(t)U(t)dt}{q \rho \Delta V}\,. \tag{7}$$

When conducting experimental studies, the main variable factors were the ratio of active load to the nominal value of the electric generator $N/N_0$ and fuel type. Each experiment was performed three times at

each power level. To determine the fuel consumption for each experiment, the same amount of fuel 2 · 10–5m$^3$ was used with time fixation.

Tables 1 and 2 show the results of the experiment and calculate the energy efficiency according to the established data of voltage and current changes (Fig. 2). When determining the useful work in the form of electricity, $\Delta P$ is determined by the trapezoidal method with the previous product of voltage and current data:

$$\Delta P = \sum_{k=1}^{N_m} \frac{U_{k-1} I_{k-1} + U_k I_k}{2} \frac{1}{f}, \quad (8)$$

where

$U_{k-1}$, $I_{k-1}$, $U_k$, $I_k$ – adjacent values of voltage and current;

$f$ – ADC channel polling frequency (1000Hz);

$N_m$ – number of measurements:

$$N_m = \Delta t \cdot f. \quad (9)$$

During the one-factor experiment, the measurement study is carried out at six power points, the power range is divided into five intervals. The number of measurements at one level is 3. Thus, 18 tests are made for each fuel, which totaled 36 tests. As the experimental curve is of the second order, six points for approximation with the required accuracy are sufficient. Also, the number of points can be justified by some sections of the curve, two rectilinear and one curvilinear, respectively, two points on the rectilinear sections and three on the curvilinear.

**Table 1.** Energy Efficiency Parameters of the Generator for Gasoline A-95 - Euro5

| No. | $\frac{N}{N_0}$ | $\Delta t$, s | $r$, g / s | *BSFC*, g / J | *BSFC*, g / (kWh) | $\Delta P$ | $\eta$ |
|---|---|---|---|---|---|---|---|
| 1 | 0 | 97 | 0.15608 | - | - | - | - |
| 2 | 0.2 | 89 | 0.17011 | 0.00033 | 1189,21 | 44828 | 0.0688 |
| 3 | 0.4 | 70 | 0.21629 | 0.00021 | 756.00 | 70693 | 0.1082 |
| 4 | 0.6 | 62 | 0.24419 | 0.00015 | 569,03 | 93320 | 0.1437 |
| 5 | 0.8 | 44 | 0.34409 | 0.00016 | 601,36 | 88843 | 0.1360 |
| 6 | 1 | 21 | 0.68818 | 0.00026 | 962,18 | 55453 | 0.0850 |

**Table 2.** Energy Efficiency Parameters of the Generator for Gasoline A-95 - Euro5 - E7

| No. | $\frac{N}{N_0}$ | $\Delta t$, s | $r$, g / s | *BSFC*, g / J | *BSFC*, g / (kWh) | $\Delta P$ | $\eta$ |
|---|---|---|---|---|---|---|---|
| 1 | 0 | 92 | 0.16457 | - | - | - | - |
| 2 | 0.2 | 84 | 0.18024 | 0.00036 | 1297,71 | 42011 | 0.0656 |
| 3 | 0.4 | 66 | 0.22939 | 0.00022 | 825,81 | 66509 | 0.1032 |
| 4 | 0.6 | 58 | 0.26103 | 0.00017 | 626,48 | 87265 | 0.1360 |
| 5 | 0.8 | 41 | 0.36927 | 0.00018 | 664,68 | 82779 | 0.1282 |
| 6 | 1 | 19 | 0.79684 | 0.00031 | 1147,45 | 47803 | 0.0742 |

From the analysis of the data given in Tables 1 and 2, it is necessary to determine the reduction of operating time of the generator $\Delta t$ and, accordingly, an increase in fuel consumption $r$ on average by 4.3 %, due to the lower calorific value of alcohol-containing gasolines.

The analysis of the data from Tables 1

and 2 is presented at the graphs of changes in specific fuel consumption and efficiency (Fig. 3). Significant specific energy consumption (1189–1297 g / (kW·h) and 962–1147 g / (kW·h)) is observed at low (0.2) and maximum load of the generator. Moreover, approaching the load to the minimum value leads to much higher unit costs than overloading the generator. The optimal load level for electric generators of this design, at which the lowest level of specific fuel consumption is expected, is 0.7 for different types and 560 and 605 g / (kW·h), respectively.

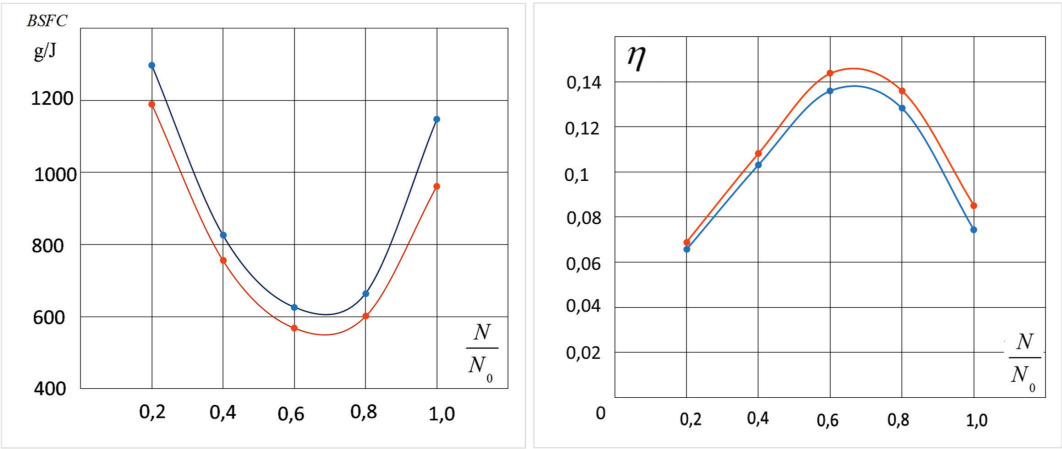


a b

*Fig. 3.* Diagrams of changes in specific fuel consumption (a) and efficiency (b) when using different types of fuels:
———- gasoline automobile A-95 - Euro5;
——— - gasoline automobile A-95 - Euro5 - E7.

The reason for these effects is a number of negative phenomena that accompany the process of electricity generation when the load deviates from the optimum. The main reasons include, in the case of increased power, deterioration of the gas filling of the cylinder, reduction of turbulence with the charge part release from the cylinder into the inlet system with increasing fuel supply. Also, costs increase in the mode close to idle to the total energy consumption $\Delta A$, when the costs of generating reactive power, which is required for generation at different load levels, is added.

An excessive use of fuel at low load is typical of most generators due to the need to maintain the frequency of the internal combustion engine, which is accompanied by the cost of friction, including aerodynamic. High specific fuel consumption at the maximum load of the generator is related to deterioration of filling of cylinders and incomplete combustion of fuel. Taking into account these features, data acquisition will be characteristic for all spark ignition generators.

The established distributions of specific values of fuel consumption and the value of the energy efficiency factor for different load levels using different fuels according to the new measurement method are necessary for modeling and planning of energy system consumption using generating units of this type.

## 4. CONCLUSIONS

The present study has proposed a new method of determining the values of fuel consumption and the value of power plant energy efficiency with two fuels (ethyl gasoline), which allows monitoring the maximum efficiency. Thus, for this equipment it is 0.147 and 0.138 at the load of 0.7 from nominal for different types of fuels. Specific costs for optimal load are 560 and 605 g / (kWh), respectively.

Under certain conditions the use of this technique, which is based on the determination of instantaneous power values, allows avoiding significant errors (30 %) in determining the energy parameters.

In addition, the experimental evaluation of the generating unit operation has confirmed that the fuel without ethanol impurities allows generating more electricity, which should be used when there is a great need.

## REFERENCES


1. Bilodid, V.D., & Taranets, K.V. (2008). Small Energy and its Importance in the Regional Systems of the Future. *Problems of General Energy, 18*, 40–47.
2. Ermilov, S. (2006). Energy Strategy of Ukraine for the Period up to 2030: Problematic Issues of Content and Implementation. *Mirror of the Week, 20*, 12.
3. Denysiuk, S., Zaichenko, S., Opryshko, V., & Derevianko, D. (2021). Assessment of Consumers Power Consumption Optimization Based on Demand Side Management. *Eureka: Physics and Engineering, 2,* 19–31.
4. Zaichenko, S., Shevchuk, S., Opryshko, V., Pryadko, S., Halem, A., & Adjebi, A. (2020). Determination of autonomous electrical energy source technical condition based on an internal combustion engine. In: *2020 IEEE KhPI Week on Advanced Technology (KhPIWeek)* (pp. 305–308), 5–10 October 2020. Kharkiv, Ukraine, IEEE.
5. Zaichenko, S., Shevchuk, S., Opryshko, V., Pryadko, S., & Halem, A. (2020). Autonomous electric power source energy efficiency improvement by internal combustion engine gases distribution control. In: *2020 IEEE 7th International Conference on Energy Smart Systems (ESS)* (pp. 262–265), 23 – 25 April 2020. IEEE.
6. Irimescu, A., Vasiu, G., & Tordai, G.T. (2014). Performance and Emissions of a Small Scale Generator Powered by a Spark Ignition Engine with Adaptive Fuel Injection Control. *Applied Energy, 121*, 196–206.
7. Keleuwani, R. S., Dube, Y., & Agbossou, K. (2018). Low-Emission Maximum-Efficiency Tracking of an Intelligent Bi-Fuel Hydrogen – Gasoline Generator for HEV Applications. *IEEE Transactions on Vehicular Technology, 67* (10), 9303–9311.
8. Onishchenko, D.O., Pankratov, S.A., Zotov, A.A., Osipkov, A.S., & Poshekhonov, R.A. (2017). Study of Influence of Hydraulic Thermoelectric Generator Resistance on Gasoline Engine Efficiency. *International Journal of Applied Engineering Research, 12* (5), 721–727.

sciendo

LATVIAN JOURNAL OF PHYSICS
AND TECHNICAL SCIENCES
2022, N 6

DOI: 10.2478/lpts-2022-0047

# STATISTICAL MODELLING OF FACTORS INFLUENCING THE AGRICULTURAL LAND MARKET IN UKRAINE

Y. Lazebnyk[1*], O. Korepanov[1], T. Chala[1], G. Korepanov[1],
D. Chernenko[1], U. Plumite[2], M. Komlieva[1]

[1] V.N. Karazin Kharkiv National University,
Department of Statistics, Accounting and Auditing,
pl. Svobody, 4, 61022, Kharkiv, UKRAINE
[6]Riga Technical University,
[2]Institute of Civil Engineering and Real Estate Economics,
6-210 Kalnciema Str., LV-1048, Riga, LATVIA
*e-mail address: y.a.lazebnyk@karazin.ua

To make informed decisions, modern society, like modern business, must operate with adequate information about many complex interrelated aspects of its activities. Land use is only one of such aspects. Agricultural lands are of particular importance today. Land data are needed to analyse environmental processes, as well as end unsystematic, uncontrolled use of agricultural land, environmental degradation, destruction of important wetlands, loss of fish diversity and destruction of wildlife habitats. To solve these problems, it is advisable to conduct regular analysis and evaluation of land resources, justification and analysis of factors influencing the agricultural land market in the country. The tasks were solved using multidimensional statistical methods, in particular, factor analysis, which helped to get rid of subjectivity in the choice of factors influencing the market under study. Based on the model of influence of factors on the national market of agricultural land in Ukraine, six main factors were identified, the most influential of which were the components of agricultural development (first factor) and, to a lesser extent, the component of vegetable production and yield (fourth factor). The interrelationships and the degree of influence of the selected factors on the main indicators of the agricultural land market, namely, on the area of purchase and sale plots, the price of purchase and sale plots, and the number of transactions were also analysed.

***Keywords*****:** *Agricultural lands, analysis of the development, factor analysis, land potential, land resources, method of principal components.*

## 1. INTRODUCTION

To make informed decisions, modern society, like modern business, must operate with adequate information about many complex interrelated aspects of its activities. Land use is only one of these aspects, but knowledge of land and soil cover continues to be increasingly important in terms of global food and energy security, environmental sustainability and economic growth.

Today agricultural lands are of particular importance. It is known that the development of infrastructure and the growing share of non-agricultural sectors of the economy significantly accelerate the process of withdrawal of land from agricultural use. This, in turn, gradually limits the area of arable land. As a result, the shortage of agricultural land is causing a decline in food production, which is exacerbated by rapid population growth in some parts of the world.

In the context of Ukraine, land data are needed to analyse environmental processes and end unsystematic, uncontrolled use of agricultural land, environmental degradation, destruction of important wetlands, loss of fish diversity and destruction of wildlife habitats. In addition, the importance of monitoring land relations is further determined by the opening of the market for agricultural land from 1 July 2021.

Given the above problems, there is a need for regular analysis and evaluation of land resources, justification factors influencing the market of agricultural land in Ukraine, thus proving the relevance of the study.

Issues related to theoretical developments and analysis of the development of the world market for agricultural land are considered in the works of such scientists as S. Balestri [1], M. Herold [2], S. Carter [2], Y. Zhang [6], H. Long [6], L. Ma [6], M. Maggioni [1], A. Menon [16], G. Robinson [9], J. Han [5], H. Lu [5], M. Vijayabaskar [3] and X. Zhang [5].

The research of B. McKay [7] and G. Oliveira [7] contributes to deepening of the understanding of land relations that go beyond the material value of land and are a way to protect national cultural identity.

Studies of C. Vaddhanaphuti [4], B. White [8], P. Vandergeest [8], E. Corbera [4], C. Park [8], L. Schoenberger [10], D. Hall [10] and C. Hunsberger [4] are devoted to the issue of harmonization of investments in agricultural lands with gender policy and climate change in some regions.

Despite the significant amount of modern research and development in this area, scientists are currently focusing on current issues of studying the current state and trends of the agricultural land market in Ukraine, which began operating in July 2021. In particular, it is important to consider the factors associated with the work of the object of study, which will assess the state of the land market in Ukraine and predict the main trends of its change.

## 2. THEORY METHODS AND METHODOLOGY

There is no doubt that the key to country's successful development, as well as its food security, is a rationally built and effective national agricultural policy, especially if the country has a powerful land potential.

In order to substantiate the state policy on the regulation of land relations, it is necessary to take into account the factors under

which the state of the agricultural land market will be formed. This problem can be solved by using multidimensional statistical methods, in particular, factor analysis and principal component analysis (PCA), which help get rid of subjectivity in the choice of factors influencing the market under study.

Large datasets are increasingly common and are often difficult to interpret. PCA is a technique for reducing the dimensionality of such datasets, increasing interpretability but at the same time minimizing information loss. It does so by creating new uncorrelated variables that successively maximize variance. Finding such new variables, i.e., the principal components, reduces to solving an eigenvalue/eigenvector problem, and the new variables are defined by the dataset at hand, not *a priori*, hence, making PCA an adaptive data analysis technique. It is adaptive in another sense too, since variants of the technique have been developed that are tailored to various different data types and structures.

The principal components method is a method by which on the basis of really existing connections of features it is possible to reveal latent generalized characteristics of organisational structure and the mechanism of development of the phenomena and processes.

With the principal component method, the effect of multicollinearity can be eliminated by replacing the initial variables, which can be correlated with fewer independent components. These so-called hypothetical quantities cannot be directly estimated.

Tasks that are put forward before the component analysis and can be solved with its help are reduced to the following [17], [18]:

- reduction of initial variables as a result of allocation of principal components;
- identification of relationships and patterns, the so-called latent effects;
- evaluation of generalized indicators (interpretation and evaluation of the main components);
- predicting the development of a particular process, when constructing a regression equation, using the results of component analysis;
- typology and classification of objects of observation;
- use of component analysis in combination with other methods of analysis, i.e. data conversion for use in other models.

The model of component analysis can be represented as follows:

$$z_i = \sum_{i=1}^{m} a_{ik} G_k, \quad (1)$$

where

$z_i$ – normalized value of the $i$-th variable with single variances;

$a_{ik}$ – weight, factor load of the $k$-th component on the $i$-th variable; i = 1, 2,…, $m$;

$k = 1, 2,\ldots, p$;

$m$ – number of variables;

$p$ – number of principal components; $p<m$;

$G_k$ – $k$-th principal component.

The algorithm of the principal components method consists of the following stages.

I. Formation of initial data matrix $X$ size $n \times m$:

$$X = \begin{bmatrix} x_{11}x_{12}x_{13}\cdots\cdots x_{1m} \\ x_{21}x_{22}x_{23}\cdots\cdots x_{2m} \\ \cdots\cdots\cdots\cdots\cdots\cdots \\ x_{n1}x_{n2}x_{n3}\cdots\cdots x_{nm} \end{bmatrix}, \quad (2)$$

where

$x_{ij}$ – the value of the $i$-th variable for the $j$-th object (observation);

i = 1, 2,…, $m$, $m$ – number of variables;

$j = 1, 2,\ldots, n$, $n$ – number of objects.

II. Calculation of the matrix of standardized values of variables, which is carried out according to the following formula:

$$z_{ij} = \frac{x_{ij} - \overline{x_i}}{\sigma_i}, \quad (3)$$

where
$z_{ij}$ – standardized value of the $i$-th variable for the $j$-th object;
$\overline{x_i}$ – the average value of the $i$-th variable;
$\sigma_i$ – standard deviation of the $i$-th variable.

III. Calculation of paired correlation coefficients matrix $R$ with "1" on the main diagonal.

IV. In the principal components method, in contrast to factor analysis, it is believed that latent components should explain all variation. Therefore, there is no need to move from a correlation matrix $R$ or a covariance matrix to a reduced covariance matrix or a reduced pair correlation matrix in which on the main diagonal instead of "1" there are communities ( $h_j^2$ ).

Thus, the next step is to calculate the diagonal matrix of eigenvalues $\Lambda$ size $p \times p$.

Inherent values $\lambda_k$ indicate the contribution of the $k$-th component to the total variance of the initial data set.

V. Calculation of the orthogonal matrix of eigenvectors size $p \times p$:

$$U = \begin{pmatrix} u_{11}u_{12}u_{13}\cdots\cdots u_{1p} \\ u_{21}u_{22}u_{23}\cdots\cdots u_{2p} \\ \cdots\cdots\cdots\cdots\cdots\cdots \\ u_{p1}u_{pk2}u_{p3}\cdots\cdots u_{pp} \end{pmatrix} \quad (4)$$

VI. Calculation of factor loads matrix $A$, the elements of which are the weight of the components (factor loads):

$$A = V \Delta^{1/2} \quad (5)$$

VII. Before moving from the matrix $A$ to the matrix of principal components values $F$, it may be necessary to find a simpler factor structure. The search for a simple factor structure is carried out using rotation procedures, as a result of which the values of some factor loads decrease and others increase. After that, a matrix of factor load after rotation is obtained.

VIII. Calculation of the matrix of principal component values $F$:

$$F = Z V \Delta^{-1/2}, \quad (6)$$

$$F = \begin{bmatrix} f_{11}f_{12}f_{13}\cdots\cdots f_{1k} \\ f_{21}f_{22}f_{23}\cdots\cdots f_{2k} \\ \cdots\cdots\cdots\cdots\cdots\cdots \\ f_{n1}f_{n2}f_{n3}\cdots\cdots f_{nk} \end{bmatrix}. \quad (7)$$

The main component method has certain properties that distinguish it from factor analysis. First, principal components are statistically independent. Second, the selected main components are ranked according to the level of their contribution to the total variance of the initial variables, i.e, the first main component has the maximum variance, the second – the largest variance among the remaining components, and so on until the full distribution of variance between the components.

Component analysis is a linear additive method. When using it, there is no need to hypothesize about the linearity of the model, the number of components and their correlation.

When using the principal components method, it is not necessary to make any assumptions about the variables, moreover – they can even be random variables.

With its help it is possible to completely decompose the variance of the initial variables, i.e., to fully explain it using latent components, which are generalized variables.

Provided that the weight of the components is determined and more than one of them – it is not always possible to unambiguously and adequately interpret the selected components. This is due to the fact that for the same components it is possible to obtain equivalent weights (loads) by their orthogonal transformation.

Transformations are performed in order to, if possible, find a simple factor structure. This is when the factor loads of traits that affect an unknown phenomenon have high values for one component and insignificant values for others. It should be noted that the element $a_{ik}$ of the factor load matrix $A$ indicates the relationship between the $i$-th initial variable and the $k$-th main component and is within the following limits: $-1 \le a_{ik} \le +1$ [17], [18]. The component for which the variables have high loads must be named, i.e., interpreted. In the case where we have more than one factor, they cannot always be interpreted unambiguously. In this regard, the factor structure can be changed using various procedures of orthogonal or oblique rotation, in the process of which the values of some factor loads increase and others decrease. The varimax procedure is most commonly used, which maximizes the variation of the factor load squares for each component by increasing the large and decreasing the factor load values. The factors that have the greatest load are given the appropriate name.

The following methods are used to select components whose solutions are easy to interpret.

1. Methods based on the rotation of factors (components) [17], [18]:

1. graphic method of rotation;
2. analytical methods:
   - varimax;
   - quartermax;
   - equimax;
   - biquartimax;

2. Methods that do not involve the rotation of components (factors).

These methods are based on the fact that before selection, the components must be specified as their number and characteristics, which must have zero weight on the components.

When deciding on the choice of the required number of components, it is advisable to use the Kaiser test or the Cattell method (the criterion of "rock collapse"). According to Kaiser's criterion, only those factors whose numbers are greater than one are left. According to Cattell's method, it is necessary to graphically display the eigenvalues of the correlation matrix in descending order. The selection of factors ends with the factor after which the inherent numbers of the correlation matrix do not decrease rapidly.

If, after taking into account, for example, 75% of the variance, the next component explains less than a given percentage of variance, it is excluded because it has too little contribution to the total variance, and therefore this component is not important.

Due to the fact that principal components are orthogonal to each other, the total variance of the $i$-th variable is equal to one. In this regard, the contribution of the $k$-th component to the total variance can be determined as follows [17], [18]:

$$\frac{\lambda_k}{m} 100\%. \tag{7}$$

The total contribution of the selected principal components or, otherwise, the completeness of the factorization is determined as follows [17], [18]:

$$\frac{\sum_{k=1}^{p} \lambda_k}{m} 100\%. \tag{8}$$

As for the significance of the weight of the components (factor loads), in socio-economic studies they can be considered significant if they are not less than a predetermined value.

For economic interpretation, only those factor loads are used, the values of which are greater 0.7 [18].

Using the theoretical provisions of factor analysis, namely, the principal compo-

nent method, the main factors influencing the market of agricultural land were identified: reduction of the space of selected features; selection of a small number of uncorrelated components that store all the information on the causal mechanism of the phenomenon; interpretation and evaluation of principal components; application of the principal components method in combination with other multidimensional methods of analysis, namely multiple regression analysis.

The model of the influence of factors on the national market of agricultural land in Ukraine was developed using regional indicators published by the State Statistics Service of Ukraine [11]–[14], which could affect researched market.

The variables in this model are defined as the average annual values of the following indicators by regions for 2015–2020:

- X1 – Present population, thousand people;
- X2 – Indices for agricultural production, %;
- X3 – Indices for crop production, %;
- X4 – Indices for livestock production, %;
- X5 – Share of regions in the agricultural production, %;
- X6 – Share of agricultural production by enterprises;
- X7 – Share of crop production, %;
- X8 – Labour productivity at enterprises that were engaged into agricultural activity (per 1 employed in agricultural production, at constant prices in 2016; thousand UAH);
- X9 – Share of regions in the crop production, %;
- X10 – Share of crop production by enterprises, %;
- X11 – Sown area for agricultural crops, thousand hectares;
- X12 – Cereals and leguminous crops output, thousand tons;
- X13 – Yields of cereals and leguminous crops, c of 1 ha;
- X14 – Sunflower production, thousand tons;
- X15 – Yields of sunflower, c of 1 ha;
- X16 – Potatoes production, thousand tons;
- X17 – Yields of potatoes, c of 1 ha;
- X18 – Vegetables crops production, thousand tons;
- X19 – Yields of vegetables crops, c of 1 ha;
- X20 – Fruit and berry crops production, thousand tons;
- X21 – Yields of fruit and berry crops, c of 1 ha;
- X22 – Share of regions in the livestock production, %;
- X23 – Share of livestock production by enterprises, %.

The average annual population in the regions of Ukraine in 2015–2020 was calculated according to the formula of the chronological average according to the current values of the indicator (at the beginning of 2015–2021) [11], [13].

Average annual indices of agricultural products, indices of crop and livestock products was calculated according to the geometric mean formula based on chain growth rates in 2015–2020 [12], [14].

Average annual labour productivity in enterprises engaged in agricultural activities in 2015–2020 was calculated as the arithmetic mean weighted by the number of the employed in agricultural production in the year [12], [14].

Average annual yields of cereals and legumes, sunflower, potatoes, vegetables, fruits and berries were calculated by the formula of the average harmonic, the numerator of which was the production of relevant crops [12], [14].

## 3. RESULTS AND DISCUSSION

Statistical model of factors influencing the market of agricultural land in Ukraine was built using the application package "STATISTICA" version 10, in particular the module "Factor Analysis".

As a result of the implementation of step-by-step procedures of factor analysis, the following results were obtained.

At the first stage, they were calculated values of eigenvalues $\lambda_j$. Principal components are those for which the Kaiser test $\lambda_j>1$ [17], [18]. Therefore, only those factors are taken into account, the inherent numbers of which are greater than one. There are six such factors (Table 1).

**Table 1.** Values of Eigenvalues and Contribution of Each of the Variances to the Total Variation of the Sign Set

| Factor | Values of eigenvalues | Proportion of total variance, % | Accumulated values of eigenvalues | Accumulated particles of total dispersion, % |
|---|---|---|---|---|
| 1 | 7.11 | 30.89 | 7.11 | 30.89 |
| 2 | 5.71 | 24.83 | 12.82 | 55.72 |
| 3 | 3.06 | 13.31 | 15.88 | 69.03 |
| 4 | 2.05 | 8.90 | 17.93 | 77.94 |
| 5 | 1.42 | 6.17 | 19.35 | 84.11 |
| 6 | 1.15 | 4.99 | 20.49 | 89.10 |

Source: Built on own calculations according to data [11]–[14].

This is also confirmed by the graphical criterion of "rock collapse" [17], [18] (Fig. 1). The six selected main components explain 89.1 % of the total variation, which indicates a high degree of factorization.

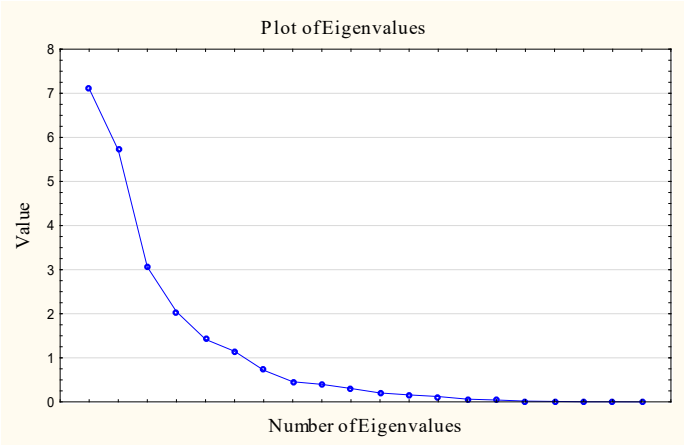


*Fig. 1.* Graphic display values of eigenvalues.
Source: Built by the authors according to their own calculations by the data [11]–[14].

Next, the factor loads were calculated, which have the meanings given in Table 2.

**Table 2.** Factor Loads before the Rotation of Factors*

| Variables | Factor 1 | Factor 2 | Factor 3 | Factor 4 | Factor 5 | Factor 6 |
|---|---|---|---|---|---|---|
| X1 | –0.110 | 0.425 | 0.416 | 0.080 | –0.049 | **0.711** |
| X2 | 0.047 | –0.587 | –0.615 | 0.357 | 0.040 | 0.132 |
| X3 | 0.212 | –0.434 | **–0.715** | 0.314 | –0.026 | 0.233 |
| X4 | –0.355 | –0.617 | 0.411 | 0.125 | 0.260 | -0.300 |
| X5 | **–0.969** | –0.015 | 0.123 | 0.162 | –0.005 | –0.107 |
| X6 | **–0.849** | 0.216 | –0.285 | –0.215 | 0.081 | 0.198 |
| X7 | –0.378 | 0.557 | –0.573 | –0.230 | –0.337 | –0.071 |
| X8 | –0.427 | **–0.593** | –0.400 | –0.052 | 0.009 | 0.280 |
| X9 | **–0.959** | 0.137 | –0.038 | 0.073 | –0.107 | –0.166 |
| X10 | **–0.797** | 0.210 | –0.400 | –0.285 | 0.018 | 0.150 |
| X11 | **–0.777** | 0.571 | –0.034 | 0.073 | –0.045 | –0.124 |
| X12 | **–0.946** | 0.115 | –0.060 | –0.091 | –0.073 | –0.169 |
| X13 | –0.395 | **–0.834** | –0.089 | –0.225 | 0.000 | –0.144 |
| X14 | –0.621 | **0.673** | –0.041 | –0.011 | 0.000 | –0.080 |
| X15 | –0.429 | **–0.829** | 0.033 | –0.215 | –0.073 | –0.052 |
| X16 | –0.371 | **–0.825** | 0.009 | 0.033 | 0.031 | 0.087 |
| X17 | –0.048 | **–0.812** | –0.165 | –0.235 | –0.340 | –0.002 |
| X18 | –0.270 | 0.271 | –0.096 | **0.834** | 0.019 | –0.080 |
| X19 | 0.084 | 0.038 | –0.468 | **0.712** | –0.258 | –0.138 |
| X20 | –0.130 | –0.296 | 0.606 | 0.290 | –0.469 | –0.052 |
| X21 | –0.137 | –0.121 | 0.397 | 0.007 | **–0.818** | 0.179 |
| X22 | –0.641 | –0.371 | 0.468 | 0.297 | 0.260 | 0.057 |
| X23 | **–0.701** | –0.129 | 0.261 | 0.206 | 0.251 | 0.390 |
| λj | 7.105 | 5.711 | 3.062 | 2.048 | 1.420 | 1.148 |
| Proportion of total variance.% | 30.9 | 24.8 | 13.3 | 8.9 | 6.2 | 5.0 |

Source: Authors' own calculations for [11]–[14].

* – Excluding the temporarily occupied territory of the Autonomous Republic of Crimea, the city of Sevastopol and a part of the temporarily occupied territories in the Donetsk and Luhansk regions.

Analysing Table 2, it is possible to determine that the obtained results are difficult to interpret and for a better understanding and correct interpretation of the results it is advisable to use the procedure of rotation of factors. "Varimax normalized" was chosen from the rotation procedures.

Inherent numbers and contribution of individual components to the total variance of the transformed factor loads are given in Table 3.

**Table 3.** Factor Loads after Rotation of Factors* (Varimax Normalized)

| Variables | Factor 1 | Factor 2 | Factor 3 | Factor 4 | Factor 5 | Factor 6 |
|---|---|---|---|---|---|---|
| X1 | 0.092 | –0.348 | 0.003 | –0.117 | 0.215 | **0.831** |
| X2 | –0.180 | 0.679 | –0.038 | 0.565 | –0.239 | –0.023 |
| X3 | –0.254 | 0.592 | –0.278 | 0.578 | –0.264 | 0.051 |
| X4 | 0.013 | 0.313 | **0.825** | –0.101 | 0.083 | –0.232 |
| X5 | **0.834** | 0.132 | 0.493 | 0.089 | 0.162 | 0.038 |
| X6 | **0.894** | 0.199 | –0.031 | –0.091 | –0.183 | 0.242 |
| X7 | **0.711** | –0.084 | –0.649 | 0.091 | –0.039 | –0.104 |
| X8 | 0.234 | **0.819** | 0.072 | 0.103 | –0.111 | 0.147 |
| X9 | **0.935** | 0.083 | 0.267 | 0.095 | 0.146 | –0.045 |
| X10 | **0.886** | 0.248 | –0.161 | –0.095 | –0.196 | 0.156 |
| X11 | **0.914** | –0.320 | 0.061 | 0.091 | 0.035 | 0.049 |
| X12 | **0.935** | 0.133 | 0.216 | –0.046 | 0.090 | –0.074 |
| X13 | 0.117 | **0.831** | 0.349 | –0.173 | 0.052 | –0.268 |
| X14 | **0.812** | –0.418 | –0.054 | 0.014 | –0.039 | 0.083 |
| X15 | 0.121 | **0.814** | 0.385 | –0.209 | 0.176 | –0.161 |
| X16 | 0.026 | **0.778** | 0.461 | 0.004 | 0.097 | 0.004 |
| X17 | –0.156 | **0.839** | –0.012 | –0.106 | 0.274 | –0.213 |
| X18 | 0.272 | –0.301 | 0.255 | **0.788** | 0.020 | 0.086 |
| X19 | –0.012 | 0.004 | –0.164 | **0.876** | 0.060 | –0.148 |
| X20 | –0.097 | 0.031 | 0.418 | 0.059 | **0.768** | 0.012 |
| X21 | 0.050 | 0.114 | –0.076 | –0.063 | **0.919** | 0.153 |
| X22 | 0.292 | 0.196 | **0.862** | 0.018 | 0.126 | 0.208 |
| X23 | 0.452 | 0.180 | 0.570 | 0.020 | 0.003 | 0.522 |
| λj | 6.616 | 4.965 | 3.402 | 2.222 | 1.897 | 1.392 |
| Proportion of total variance.% | 28.8 | 21.6 | 14.8 | 9.7 | 8.2 | 6.1 |

Source: Authors' own calculations for [11]–[14].

* – Excluding the temporarily occupied territory of the Autonomous Republic of Crimea, the city of Sevastopol and a part of the temporarily occupied territories in the Donetsk and Luhansk regions.

As can be seen from Table 3, the contribution of the first component in the total variance of the data set is 28.8 %, the second – 21.6 %, the third – 14.8 %, the fourth – 9.7 %, the fifth – 8.2 %, the sixth – 6.1 %. Together, these components account for almost 89.2 % of the total variation, which indicates a high level of factorization. Note that the first component is closely related to the variables: X5, X6, X7, X9, X10, X11, X12, X14. Thus, the first component can be interpreted as a generalized factor in the development of agriculture with an emphasis on crop production. Another component is closely related to the variables: X8, X13, X15, X16. It is interpreted as a factor in the intensive development of agriculture. The third component is closely related to the following variables: X4, X22. It can be interpreted as a factor in rural development livestock. The fourth component is closely related to the variables: X18, X19. It is interpreted as a factor in the production and yield of vegetable crops. The fifth compo-

nent is closely related to the variables: X20, X21. It is interpreted as a factor in the production and yield of fruit and berry crops. The sixth component is closely related to the variable: X1. It is interpreted as a factor in the size of the existing population. The values of principal components for the regions of Ukraine are given in Table 4.

**Table 4.** Values of Principal Components for the Regions of Ukraine*

| Region (oblast) | Factor 1 | Factor 2 | Factor 3 | Factor 4 | Factor 5 | Factor 6 |
|---|---|---|---|---|---|---|
| Vinnytska | 1.002 | 0.498 | 2.413 | 0.240 | 1.179 | –0.352 |
| Volynska | –1.145 | 0.495 | 0.192 | 0.231 | –0.870 | 0.392 |
| Dnipropetrovska | 0.698 | –1.023 | 1.019 | 1.034 | 0.061 | 1.807 |
| Donetska | –0.462 | –1.084 | –0.400 | –1.306 | 0.606 | 2.867 |
| Zhytomyrska | –0.302 | 1.128 | –0.530 | 0.767 | –0.050 | –0.335 |
| Zakarpatska | –2.363 | –1.189 | 0.728 | –0.003 | 0.521 | –1.470 |
| Zaporizhska | 0.339 | –1.073 | –0.654 | 0.324 | –0.808 | 0.301 |
| Ivano–Frankivska | –1.605 | 0.291 | 0.591 | –0.655 | –1.195 | 0.106 |
| Kyivska | 0.331 | 0.184 | 1.616 | –0.219 | –0.531 | 0.390 |
| Kirovohradska | 0.946 | –0.945 | –0.070 | –1.332 | –1.075 | –1.467 |
| Luhanska | –0.211 | 0.019 | –2.627 | –0.051 | 0.074 | 1.042 |
| Lvivska | –1.030 | 0.885 | 0.515 | 0.657 | –0.165 | 1.185 |
| Mykolayivska | 0.519 | –1.465 | –0.630 | 0.795 | –0.750 | –1.162 |
| Odeska | 0.779 | –1.856 | –0.558 | –1.883 | 0.881 | –0.572 |
| Poltavska | 1.319 | 0.520 | –0.324 | 0.206 | 2.085 | –0.450 |
| Rivnenska | –1.027 | 0.865 | –0.496 | 0.021 | 0.454 | –0.084 |
| Sumska | 0.758 | 1.353 | –0.492 | –0.615 | –1.476 | –0.517 |
| Ternopilska | –0.047 | 1.101 | –0.493 | –0.037 | 0.331 | –0.406 |
| Kharkivska | 1.035 | –0.104 | –0.082 | 0.637 | 0.464 | 0.462 |
| Khersonska | 0.261 | –1.121 | –0.213 | 3.184 | –0.523 | –0.435 |
| Khmelnytska | 0.543 | 1.374 | –0.399 | –0.099 | 1.745 | –0.203 |
| Cherkaska | 0.566 | 0.043 | 1.565 | –1.139 | –0.928 | 0.268 |
| Chernivetska | –1.696 | –0.233 | –0.071 | –0.337 | 1.412 | –1.069 |
| Chernihivska | 0.793 | 1.337 | –0.601 | –0.421 | –1.443 | –0.297 |

Source: Authors' own calculations for [11]–[14].

* – Excluding the temporarily occupied territory of the Autonomous Republic of Crimea, the city of Sevastopol and a part of the temporarily occupied territories in the Donetsk and Luhansk regions.

Estimates of principal components are used to measure the relationship and study the impact of selected factors on the main indicators of the agricultural land market, namely, the area of plots for sale from 01.07.2021 to 16.01.2022, ha ($Y_1$), the price of plots of land for sale for the period from 01.07.2021 to 16.01.2022, UAH per hectare ($Y_2$), and the number of transactions for the period from 01.07.2021 to 16.01.2022 ($Y_3$).

Describing the matrix of correlation coefficients for the three dependent (area of sales, price, and number of transactions) and independent variables (factors), it should be noted the high level of correlation (positive relationship) between the dependent variables of the number and area of sales is a logical explanation of the mechanism of functioning of the market of agricultural lands and the specifics of reporting data on it (Table 5).

**Table 5.** Correlation Coefficients between the Main Indicators of the Agricultural Land Market and the Selected Factors

| | $Y_1$ | $Y_2$ | $Y_3$ |
|---|---|---|---|
| $Y_1$ | 1.00 | | |
| $Y_2$ | –0.22 | 1.00 | |
| $Y_3$ | 0.88 | –0.13 | 1.00 |
| Factor 1 | 0.62 | –0.17 | 0.70 |
| Factor 2 | –0.25 | 0.24 | 0.10 |
| Factor 3 | –0.05 | 0.39 | 0.05 |
| Factor 4 | 0.41 | –0.05 | 0.28 |
| Factor 5 | 0.04 | 0.00 | 0.06 |
| Factor 6 | 0.08 | 0.22 | –0.04 |

Source: Authors' own calculations for [11]–[14].

An increase in the number of transactions leads to an increase in the total area of sales plots, but this relationship may not be fully functional, because the area of individual transactions is different and can vary significantly. In addition, despite the low in absolute terms statistically insignificant correlation between the area of purchase and sale and their price, the negative direction of this relationship is clear and is interpreted in the laws of supply and demand – at a high price fewer land transactions and increase in the total area of land sold (increase in supply) lead to a gradual decline in market prices for agricultural land.

Regarding the relationships between independent and dependent variables, there are high enough correlation coefficients for the first factor (first component) in the equations with the area and number of sales transactions. Since the first component is interpreted as a generalized factor in the development of crop production, this correlation characterises the main targeted use of agricultural land in Ukraine and confirms the market activity of those companies that are primarily related to crop production.

Using regression analysis to study the impact of the six main components (factors) of agriculture identified above, three main models were built to characterise each of the three dependent variables separately.

The multiple regression equation looks like this:

$$Y_i = a_0 + a_1 G_1 - a_2 G_2 - a_3 G_3 + a_4 G_4 + a_5 G_5 + a_6 G_6, \quad (9)$$

where
$Y_i$ – theoretical values of the chosen ones;
$a_0$ – initial regression parameter;
$a_j$ – regression parameter of the factor $G_j$, $i = 1, \ldots, 6$;
$G_j$ – factor selected by the principal components method, $i = 1, \ldots, 6$.

The first regression model considers the effect of six factors on the area of purchase and sale. The significance of the coefficients of the model was estimated in Excel using the statistical procedure Regression in the Data Analysis package. The results of the calculations are presented in Table 6.

**Table 6.** Characteristics of the Regression Model Areas of Plots of Sale of Agricultural Land in Ukraine ($y_1$)

| **Regression Statistics** | | | | | | |
|---|---|---|---|---|---|---|
| **Multiple R** | 0.789 | | | | | |
| **R Square** | 0.624 | | | | | |
| **Adjusted R Square** | 0.491 | | | | | |
| **Standard Error** | 3183.118 | | | | | |
| **Observations** | 24 | | | | | |
| **ANOVA (Analysis of variance)** | | | | | | |
| | ***df*** | ***SS*** | ***MS*** | ***F*** | ***Significance F*** | |
| **Regression** | 6 | 285839766.3 | 47639961.06 | 4.702 | 0.00539 | |
| **Residual** | 17 | 172248090.4 | 10132240.61 | | | |
| **Total** | 23 | 458087856.7 | | | | |
| | ***Coefficients*** | ***Standard Error*** | ***t Statistics*** | ***P-value*** | ***Lower 95%*** | ***Upper 95%*** |
| **Y-section** | 4398.97 | 649.751 | 6.770 | 0.0000 | 3028.12 | 5769.83 |
| **Factor 1** | 2765.24 | 663.726 | 4.166 | 0.0006 | 1364.90 | 4165.58 |
| **Factor 2** | –1104.27 | 663.726 | –1.664 | 0.1145 | –2504.61 | 296.07 |
| **Factor 3** | –217.29 | 663.726 | –0.327 | 0.7474 | –1617.63 | 1183.05 |
| **Factor 4** | 1827.38 | 663.726 | 2.753 | 0.0136 | 427,04 | 3227.72 |
| **Factor 5** | 188.23 | 663.726 | 0.284 | 0.7801 | –1212.11 | 1588.57 |
| **Factor 6** | 374.01 | 663.726 | 0.563 | 0.5805 | –1026.33 | 1774.35 |

Source: Authors' own calculations for [15], [11]–[14].

Checking the materiality of the connection is statistically formulated as a test of null hypotheses: $H_0$: $R^2 = 0$; $H_0$: $a_j = 0$. Hypothesis $H_0$ is rejected or accepted on the basis of statistical criteria, in particular the variance *F*-criterion, the statistical characteristic of which is calculated by the ratio of estimates of factor and residual variances [17], [18]. Critical values $F_{1-\alpha}(k_1, k_2)$, where α – the materiality level, $k_1 = m–1$, $k_2 = n–(m–1)$ – the number of freedom degrees of the numerator and denominator was determined using the EXCEL FINV function. In our case $F_{emp.} = 4.7 > F_{crit.}$ (1–α; $k_1$; $k_2$) = 2.77.

The strength of the connection can be inferred from the value of the coefficient of determination $R^2$. For the model obtained (Table 6):

- close to unity coefficient of determination $R^2 = 0.62$,
- the estimated value of *F*-statistics ($F_{emp.} = 4.7$) is more than critical $F_{åmp.} = 4.7 > F_{crit.} = 2.7$, which indicates the high adequacy of the constructed model.

The analysis allows us to conclude that the constant $a_0$ and the coefficient $a_1$ and $a_4$ are significant, because the absolute values of their *t*-statistics are more than covered, because the hypothesis $H_0$ at the level of significance $\alpha$ deviates if the inequality $t_{emp.} > t_{crit.1-\alpha;\, n-m-1}$ holds, where $t_{emp.}$ is calculated and $t_{crit.\varepsilon;n-m-1}$ is determined from the table of theoretical values of the *t*-test at the level of significance α and (*n*–*m*–1) degrees of freedom. Theoretical significance of the *t*-test $t_{crit.}$ was obtained using the function EXCEL T.INV.2T ((1–α), *n*–*m*–1) = T.INV.2T (0,05, 24–6–1) = 2.11 (for two-way distribution).

Therefore, the equation of multiple

regression on the selected factors is as follows:

$$Y_1 = 4398.9+2765.2\ G_1–1104.2\ G_2–217.3\ G_3+1827.4\ G_4+188.2\ G_5+374\ G_6.$$

Considering the regression coefficients on the factors, it is seen that only the first (generalized factor of agricultural development with an emphasis on crop production) and the fourth (factor of production and yield of vegetable crops) factors affect the area of purchase and sale, because *t*-statistics of these coefficients are higher than the corresponding tabular value of 2.11 for 95 % of the confidence interval.

The significance of the other four factors has not been confirmed. Thus, we can talk about the real positive (due to the sign of the coefficient) impact of the first and fourth main components on the area of purchased/sold plots of agricultural land in Ukraine.

Analysing the second regression model (Table 7), which describes the impact of six components on the price of plots of sale, no statistically significant effect was found.

**Table 7.** Characteristics of the Regression Model Prices of Plots for Sale of Agricultural Land in Ukraine ($y_2$)

| **Regression Statistics** | | | | | | |
|---|---|---|---|---|---|---|
| **Multiple R** | 0.540 | | | | | |
| **R Square** | 0.292 | | | | | |
| **Adjusted R Square** | 0.042 | | | | | |
| **Standard Error** | 13155.943 | | | | | |
| **Observation** | 24 | | | | | |
| **ANOVA (Analysis of variance)** | | | | | | |
| | ***df*** | ***SS*** | ***MS*** | ***F*** | ***Significance F*** | |
| **Regression** | 6 | 1213657674 | 202276279.0 | 1.169 | 0.368 | |
| **Residual** | 17 | 2942340659 | 173078862.3 | | | |
| **Total** | 23 | 4155998333 | | | | |
| | ***Coefficients*** | ***Standard Error*** | ***t Statistics*** | ***P-value*** | ***Lower 95 %*** | ***Upper 95 %*** |
| **Y-section** | 35604.25 | 2685.446 | 13.258 | 0.0000 | 29938.45 | 41270.05 |
| **Factor 1** | –2319.53 | 2743.204 | –0.846 | 0.4095 | –8107.18 | 3468.13 |
| **Factor 2** | 3289.55 | 2743.204 | 1.199 | 0.2469 | –2498.11 | 9077.20 |
| **Factor 3** | 5230.39 | 2743.204 | 1.907 | 0.0736 | –557.26 | 11018.05 |
| **Factor 4** | –738.84 | 2743.204 | –0.269 | 0.7909 | –6526.49 | 5048.82 |
| **Factor 5** | 41.56 | 2743.204 | 0.015 | 0.9881 | –5746.09 | 5829.22 |
| **Factor 6** | 2943.09 | 2743.204 | 1.073 | 0.2983 | –2844.56 | 8730.74 |

Source: Authors' own calculations for [15], [11]–[14].

The third regression model examines the effect of six factors on the number of sales transactions, and the results of the calculations are presented in Table 8.

**Table 8.** Characteristics of the Regression Model and the Number of Transactions of Purchase and Sale of Agricultural Land in Ukraine ($y_3$)

| **Regression statistics** | | | | | | |
|---|---|---|---|---|---|---|
| **Multiple R** | 0.765 | | | | | |
| **R Square** | 0.585 | | | | | |
| **Adjusted R Square** | 0.439 | | | | | |
| **Standard Error** | 729.180 | | | | | |
| **Observation** | 24 | | | | | |
| **ANOVA (Analysis of variance)** | | | | | | |
| | ***df*** | ***SS*** | ***MS*** | ***F*** | ***Significance F*** | |
| **Regression** | 6 | 12764336.55 | 2127389.43 | 4.001 | 0.011 | |
| **Residual** | 17 | 9038957.29 | 531703.37 | | | |
| **Total** | 23 | 21803293.83 | | | | |
| | ***Coefficients*** | ***Standard Error*** | ***t Statistics*** | ***P-value*** | ***Lower 95%*** | ***Upper 95%*** |
| **Y-section** | 1210.08 | 148.843 | 8.130 | 0.000 | 896.056 | 1524.115 |
| **Factor 1** | 680.73 | 152.045 | 4.477 | 0.000 | 359.949 | 1001.521 |
| **Factor 2** | 97.51 | 152.045 | 0.641 | 0.530 | –223.276 | 418.296 |
| **Factor 3** | 53.10 | 152.045 | 0.349 | 0.731 | –267.683 | 373.889 |
| **Factor 4** | 272.92 | 152.045 | 1.795 | 0.090 | –47.863 | 593.709 |
| **Factor 5** | 59.42 | 152.045 | 0.391 | 0.701 | –261.365 | 380.207 |
| **Factor 6** | –35.00 | 152.045 | –0.230 | 0.821 | –355.790 | 285.782 |

Source: Authors' own calculations for [15], [11]–[14].

The adequacy of such a model is slightly lower ($R^2 = 0.585$) than when determining the effects of components on the area of purchase and sale, but the actual value of the *F*-criterion is greater than the *F* tabular (4.0 > 2.77), so the model is statistically significant and in general it describes 58.5 % of the variation in the dependent variable. The multiple regression equation looks like this:

$$Y_3 = 1210.08+680.73G_1+97.50G_2+53.10G_3 +272.92G_4+59.42G_5–35G_6.$$

Unlike the first model, the regression coefficient for the factor of production and yield of vegetable crops (component four) is no longer statistically significant at 95 % confidence interval, and only the influence of the factor of agricultural development with emphasis on crop production remains different from zero (value of *t*-statistics of 4.48 is higher than the corresponding table value of 2.11). Thus, the impact of the six studied components on the three main indicators of the market of purchase and sale of agricultural land in Ukraine is limited mainly by the effects of the agricultural development component, and the development and dynamics of land prices are formed entirely without the influence of all identified components.

## 4. CONCLUSIONS

The generalization of the theoretical foundations of the basic concepts and categories used in the study has allowed us to determine that relevant to the research topic is the category of agricultural land, which, in turn, is divided into agricultural and non-agricultural land. Both types of land are subject to the land market in Ukraine through the NMV mechanism, but the level of statistical reporting and availability of information on the latter is insufficient compared to the former, which requires improved approaches to collecting and disseminating relevant statistical information.

Factor analysis proves a statistically significant impact of two of the six most important selected agricultural components (agricultural development components (first factor) and to a lesser extent vegetable production and yield component (fourth factor)) on the number and area of agricultural land sales in Ukraine. None of the considered components, however, has a statistically significant impact on the development of prices for agricultural land.

## REFERENCES


1. Balestri, S., & Maggioni, M. A. (2017). This Land is my Land! Large-Scale Land Acquisitions and Conflict Events in Sub-Saharan Africa. *2017 World Bank Conference on Land and Poverty.* Washington DC. 20–24 March 2017. Available at https://www.researchgate.net/publication/314871867_This_land_is_my_land_Large-Scale_Land_Acquisitions_and_conflict_events_in_Sub-Saharan_Africa
2. Carter, S., Manceur, A. M., Seppelt, R., Hermans-Neumann, K., Herold, M., & Verchot, L. (2017). Large-Scale Land Acquisitions and REDD+: A Synthesis of Conflicts and Opportunities. *Environmental Research Letters*, *12* (3). Available at https://www.cifor.org/publications/pdf_files/articles/ACarter1802.pdf
3. Cherniak, O. I., & Kudinenko, M. Ya. (2002). Analysis and Forecast of Ukraine's GDP Dynamics Using the Method SSA (in Ukrainian). *Ekonomika i prohnozuvannia*, *4*, 134–147. Institute of Economics and Forecasting. Kyiv [Online]. Available at https://econom.univ.kiev.ua/wp-content/uploads/science/articles/Chernyak_OI/Analiz_ta_prognoz_dynamiky_VVP_Urainy_za_dopomogou_metody_SSA.pdf
4. Corbera, E., Hunsberger, C., & Vaddhanaphuti, C. (2017). Climate Change Policies, Land Grabbing and Conflict: Perspectives from Southeast Asia. *Canadian Journal of Development Studies, 38* (3)*,* 297–304.
5. Han, J., Jiang, M., Zhang, X., & Lu, X. (2021). Knowledge Mapping Analysis of Transnational Agricultural Land Investment Research. *Land Use Policy*, *10* (12). Available at https://www.mdpi.com/2073-445X/10/12/1374/htm
6. Long, H., Zhang, Y., Ma, L., & Tu, S. (2021). Land Use Transitions: Progress, Challenges and Prospects. *Land Use Policy*, *10* (9). Available at https://webcache.googleusercontent.com/search?q=cache:jBzxLcxZSZkJ:https://www.mdpi.com/2073-445X/10/9/903/pdf+&cd=2&hl=ru&ct=clnk
7. McKay, B. M., Oliveira, G. d. L. T., & Liu, J. (2020). Authoritarianism, Populism, Nationalism and Resistance in the Agrarian South. *Canadian Journal of Development Studies*, 41, 347–362.
8. Park, C. M. Y., & White, B. (2017). Gender and Generation in Southeast Asian Agro-commodity Booms. *The Journal of Peasant Studies*, 1103–1110.

9. Robinson, G.M., & Carson, D.A. (2015). The Globalisation of Agriculture: Introducing the Handbook. *Annu Rev Resour Econ*., 1–28.
10. Schoenberger, L., Hall, D., & Vandergeest, P. (2017). What Happened when the Land Grab Came to Southeast Asia? *The Journal of Peasant Studies*, *44*, 697–725.
11. State Statistics Service of Ukraine. (2022). *Rehiony Ukrainy 2019. Statystychnyj zbirnyk [Regions of Ukraine 2019. Statistical yearbook]* (in Ukrainian), section 1, Derzhkomstat, Kyiv, Ukraine. Available at http://www.ukrstat.gov.ua/druk/publicat/kat_u/2019/zb/12 /zb_ru1ch2019.pdf
12. State Statistics Service of Ukraine. (2022). *Rehiony Ukrainy 2019. Statystychnyj zbirnyk [Regions of Ukraine 2019. Statistical yearbook]*, section 2, Derzhkomstat, Kyiv, Ukraine. Available at http://www.ukrstat.gov.ua/druk/publicat/kat_u/2019/zb/12/zb_ru2ch2019.pdf
13. State Statistics Service of Ukraine. (2022). *Rehiony Ukrainy 2020. Statystychnyj zbirnyk [Regions of Ukraine 2020. Statistical yearbook]* (in Ukrainian), section 1, Derzhkomstat, Kyiv, Ukraine. Available at https://ukrstat.org/uk/druk/publicat/kat_u/2021/zb/12/Regionu_20_pdf.zip
14. State Statistics Service of Ukraine. (2022). *Rehiony Ukrainy 2020. Statystychnyj zbirnyk [Regions of Ukraine 2020. Statistical yearbook]* (in Ukrainian), section 2, Derzhkomstat, Kyiv, Ukraine. Available at https://ukrstat.org/uk/druk/publicat/kat_u/2021/zb/12/Regionu_20_pdf.zip
15. The Official Agricultural and Political Site of Ukraine. (2022). *Land Market in Ukraine. Map of Land Agreements and Land Prices from July 1, 2021* (in Ukrainian). Available at https://agropolit.com/spetsproekty/892-rinok-zemli-v-ukrayini-mapa-zemelnih-ugod-i-tsin-na-zemlyu-z-1-lipnya-2021-roku?utm_source=kurkul&utm_medium=news
16. Vijayabaskar, M., & Menon, A. (2018). Dispossession by Neglect: Agricultural Land Sales in Southern Indian. *J. Agrar. Chang.*, 18, 571–587.
17. Yerina, A.M. (2001). *Statystychne modeliuvannia ta prohnozuvannia* [Statistical modelling and forecasting] (in Ukrainian): navch. posib. KNEU, Kyiv, Ukraine.
18. Yerina, A.M., & Yerin, D.L. (2014). *Statystychne modeliuvannia ta prohnozuvannia* [Statistical modelling and forecasting] (in Ukrainian): navch. posib. KNEU, Kyiv, Ukraine.